Clim Dyn (2016) 47:3713–3736
DOI 10.1007/s00382-016-3038-2

Changes in the boreal summer intraseasonal oscillation projected by the CNRM-CM5 model under the RCP 8.5 scenario

Jianying Li[1,3] · **Jiangyu Mao**[1,2]

Received: 12 August 2015 / Accepted: 11 February 2016 / Published online: 20 February 2016
© Springer-Verlag Berlin Heidelberg 2016

Abstract The 30–60-day boreal summer intraseasonal oscillation (BSISO) is the predominant intraseasonal variability in the Asian summer monsoon (ASM) region, representing the canonical northward and northwestward propagating convective components over South Asia (SA) and East Asia/western North Pacific (EA/WNP) sectors in conjunction with eastward propagating convective anomalies. The objective of this study is to assess possible changes of the 30–60-day BSISO in future global warming condition by comparing the twentieth century simulation with the twenty-first century projection produced by the CNRM-CM5 model under the representative concentration pathway 8.5 (RCP 8.5) scenario. In response to the increase of sea surface temperature in the tropical and subtropical Indian and Pacific Oceans, the saturation specific humidity in the planetary boundary layer (PBL) increases by about 16 %, providing more moisture and moist static energy for tropical convection. Thus, the BSISO will be intensified, with large-amplitude events prevailing in a broader range of the Indo-Pacific region. The convective signal will initiate over more westward parts of the Indian Ocean and decay over the more eastward tropical Pacific. As the strengthening of northward propagations over the SA and EA/WNP sectors is intimately related to equatorial enhanced convective anomalies, the enhanced convective anomalies are accompanied by stronger ascents on the top of the PBL, together with the wetter seasonal-mean PBL background, resulting in stronger northward propagations through moisture mechanisms. Moreover, due to the increased moisture-holding capacity of the low-level atmosphere, the phase speeds of SASM and EA/WNP northward propagation will decrease.

Keywords Boreal summer intraseasonal oscillation · Climate change · Global warming · CNRM-CM5 model · Increased SST

1 Introduction

The Fifth Assessment Report (AR5) by the Intergovernmental Panel on Climate Change (IPCC 2013) suggests that the trend of global warming will continue in the twenty-first century even under the lowest greenhouse gas concentration scenario of the representative concentration pathway 2.6 (RCP 2.6). Due to the inertia of climate systems, the global mean surface temperature for 2081–2100 relative to 1986–2005 is projected to possibly increase at least in the range of 0.3–1.7 °C. Under this global warming projection, changes in the boreal summer rainfall will not be uniform, with rainfall over the Asian monsoon areas likely to increase (Turner and Annamalai 2012; Seo et al. 2013), while rainfall over mid-latitude and subtropical dry regions are likely to decrease. As an important indicator of the Asian summer monsoon (ASM), the significant increase in the ASM rainfall implies a modification to the Asian monsoon climate system. Besides the seasonal variation, the ASM also possesses considerable variability on a wide range of timescales. Within the annual cycle, intra-seasonal

---

✉ Jiangyu Mao
mjy@lasg.iap.ac.cn

[1] State Key Laboratory of Numerical Modeling for Atmospheric Sciences and Geophysical Fluid Dynamics (LASG), Institute of Atmospheric Physics, Chinese Academy of Sciences, P.O. Box 9804, Beijing 100029, China

[2] Joint Center for Global Change Studies, Beijing 100875, China

[3] University of Chinese Academy of Sciences, Beijing 100049, China

oscillation is a dominant variability of the ASM, characterized by several active and break sequences occurring within each summer season (Webster et al. 1998; Mao et al. 2010). An ill-timed active episode or lull in the monsoon rains may have devastating effects on agriculture even if the summer seasonal-mean rainfall is normal (Webster et al. 1998). Therefore, assessing potential impacts of global warming on the boreal summer intraseasonal oscillation (BSISO) over the entire ASM area is of great importance.

Compared to its wintertime counterpart, the Madden–Julian Oscillation (MJO; Madden and Julian 1971, 1972), BSISO over the ASM region has a more complex structure (e.g., Sperber et al. 2013), with northward propagation of convective anomalies over the South Asia (SA) sector in conjunction with the eastward propagation (Wang and Xie 1997; Annamalai and Slingo 2001; Jiang et al. 2004; Zhang 2005; Lee et al. 2013), and the northwestward propagation over the East Asia/western North Pacific (EA/WNP) sector (Annamalai and Slingo 2001; Kemball-Cook and Wang 2001; Seo et al. 2007; Mao et al. 2010; Lee et al. 2013). Such complex propagations result in regional heat sources and sinks (Annamalai and Slingo 2001), particularly a northwest to southeast tilted rainband (Sperber and Annamalai 2008). Over the SA summer monsoon (SASM) region, there are two prominent modes within the broad range of subseasonal periods, one being the 10–20-day westward propagating mode (Krishnamurti and Ardanuy 1980; Chen and Chen 1993; Fukutomi and Yasunari 1999) and another being 30–60-day oscillation with striking northward propagation from 5°S to 25°N (Yasunari 1980; Wang and Rui 1990; Jones et al. 2004). The intraseasonal variations over the EA/WNP monsoon region are also controlled primarily by 30–60-day and/or 10–20-day oscillations (Lau et al. 1988; Annamalai and Slingo 2001; Mao and Chan 2005).

As an integrated system, the 30–60-day BSISO is characterized by the quadrupole pattern (Kemball-Cook and Wang 2001; Annamalai and Sperber 2005; Seo et al. 2007; Lee et al. 2013): active (suppressed) convection anomalies dominate the Indian subcontinent and extend over the Bay of Bengal (BOB), maritime continent and equatorial western Pacific (EWP; 5°S–5°N, 100°–140°E), while convection anomalies with the opposite sign occupy the equatorial Indian Ocean (EIO; 5°S–5°N, 70°–100°E) and WNP (10°–20°N, 100°–140°E). This quadrupole structure, which indicates the 30–60-day BSISO along the Indian and western Pacific longitudes being interactive and intertwined, arises from the complex propagations over the entire ASM region. As shown in Lee et al. (2013), the northward propagation over the SASM area leads to the south-north oriented dipole pattern between the EIO and the Indian subcontinent–BOB. Similarly, the northward/northwestward propagation over the EA/WNP area gives rise to another dipole pattern. The equatorial eastward propagation from the Indian Ocean to the western Pacific connects the dipole over the Indian longitudes with the complementary dipole over the EA/WNP sector (e.g., Annamalai and Sperber 2005), thus forming the quadrupole pattern.

The 10–20-day BSISO mode features an elongated and front-like convection band extending from the WNP through the South China Sea (SCS) to the EIO, with a northeast to southwest slope (Lee et al. 2013). Since the evolution of 10–20-day BSISO greatly differ from that of the 30–60-day BSISO, changes of these two intraseasonal modes should be discussed separately. In the present study, we mainly focused on how the 30–60-day BSISO will behave in the warmed climate.

So far, most studies have paid more attention to the possible changes of the boreal wintertime MJO in a warmer climate system (Jones and Carvalho 2011; Liu 2013; Yang et al. 2013; Subramanian et al. 2014), while how and to what extent BSISOs will be modified under global warming conditions have not been investigated. While the wintertime MJO is mainly confined to the equatorial areas, BSISOs propagate poleward prominently over monsoon regions, thereby influencing the ASM monsoonal weather and climate more directly (Goswami et al. 2003; Bhat 2006; Ko and Hsu 2006, 2009; Ding and Wang 2009; Li et al. 2015). BSISOs are noted to modulate the occurrences of extreme synoptic events, especially the genesis of tropical cyclones (Goswami et al. 2003; Ko and Hsu 2006, 2009). They are also responsible for seasonal-mean droughts or floods (Bhat 2006; Ding and Wang 2009; Li et al. 2015). Therefore, studying the modifications of BSISOs in the future climate has profound implications.

Yang et al. (2013) and Sabeerali et al. (2014) suggested that the northward propagating BSISO over the SASM area will intensify under the global warming condition due to the enhanced air-sea interaction. Sabeerali et al. (2014) also found that the northward propagation tends to slow down and attributed this change of phase speed to the reduced easterly vertical shear and the reduced moisture gradient across the equator. However, changes of BSISOs over the EA/WNP area are unclear. Moreover, because BSISOs over the SASM and EA/WNP areas are interconnected, modifications of the spatial distribution and life cycle evolution over the entire ASM region deserve further investigation.

Because coupled general circulation models (CGCMs) are essential tools for predicting future climate change, the ability of a CGCM to realistically simulate the present-day climate is very important for the reliability of climate projections. Although current models still have difficulties in simulating all characteristics of BSISOs (Waliser et al. 2003; Lin et al. 2008), great improvements have been made from the third to the fifth phases of the Coupled Model Inter-comparison Project (CMIP3 to CMIP5) (Hung et al.

2013; Sperber et al. 2013). The CNRM-CM5 model stands out among the CMIP5 models for the following reasons. First, the CNRM-CM model has long been one of the few CGCMs participating in the CMIP3 and CMIP5 that has a reasonable representation of the MJO (Lin et al. 2006; Hung et al. 2013; Jiang et al. 2015). This CGCM captures the realistic vertical structures of key dynamical and thermodynamical variables, which are essential for a quality representation of MJO. It can realistically represent the interactions between small-scale cumulus convection and large-scale circulation, with such interactions being the core of intraseasonal oscillation theory. Second, Sperber et al. (2013) and Sabeerali et al. (2013) stated that the CNRM-CM5 model produced a reasonable pattern of the seasonal-mean rainfall and 850-hPa winds during the boreal summer, with a high resemblance to the observations. Again, as the simulation performance of BSISOs depends on realistic reproduction of the seasonal-mean ASM circulation (Ajayamohan and Goswami 2007), the results of Sperber et al. (2013) and Sabeerali et al. (2013) provide another piece of evidence that the CNRN-CM5 model has priority in simulating the BSISOs. Third, Sabeerali et al. (2013) and Jiang et al. (2015) showed that the CNRM-CM5 model not only captures the 30–60-day eastward propagation over the EIO but also reproduces the secondary amplification over the EWP and the eastward movement beyond 100°E, while most of the other CMIP5 models fail to simulate the eastward propagation east of 100°E. This reasonable representation of 30–60-day BSISO in the CNRM-CM5 model suggests that the simulation results of this model are reliable for studying the changes of 30–60-day BSISO over the ASM region in a global warming scenario.

Because most of the existing work about the changes of intraseasonal oscillations under the global warming scenario is mainly focused on the wintertime MJO or BSISO over the SASM area, paying less attention to the BSISO over the EA/WNP region, the objective of the present study is to investigate the possible changes of the 30–60-day BSISO over the entire ASM region, in terms of spatial distribution and propagation characteristics. We approach this goal by conducting a comparative analysis between the historical run (also referred to as "twentieth century simulation") and the global warming projections (also referred to as "twenty-first century simulation") by the CNRM-CM5 model.

Section 2 briefly describes the CNRM-CM5 model, the observational datasets, and the methods used to diagnose the modifications of the 30–60-day BSISO. The changes in summertime seasonal-mean climate in terms of dynamical and hydrological fields in a global warming scenario are outlined in Sect. 3. Section 4 presents the changes of the 30–60-day mode in the warmed climate and provides related mechanisms for the changes. Finally, a summary and discussion are given in Sect. 5.

2 Model simulations and methods

2.1 CNRM-CM5 model

The CNRM-CM5 is the new version (Voldoire et al. 2013) of the CGCM (CNRM-CM) developed jointly by CNRM-GAME (Centre National de Recherches Météorologiques-Grouped'études de l' Atmosphère Météorologique) and Cerfacs (Centre Européen de Rechercheet de Formation Avancée). The atmospheric component of CNRM-CM5 is a spectral model that operates on a T127 triangular truncation, equivalent to a spatial resolution of about 1.4° in both longitude and latitude, with 31 vertical layers. The oceanic component is based on the ocean part of the Nucleus for European Modelling of the Ocean (Madec 2008). The atmospheric, oceanic, and other components (the land surface and sea ice models) are run as separate executables, with the OASIS3 coupler (Valcke 2006) used to synchronize, interpolate and exchange the coupling fields.

Compared with the previous version CNRM-CM3, CNRM-CM5 has improved dynamics and physical parameterizations (Voldoire et al. 2013). Horizontal resolution was increased both in the atmosphere (from 2.8° to 1.4°) and in the ocean (from 2° to 1°) components. A new long-wave radiation scheme (Mlawer et al. 1997) was introduced, and the treatments of tropospheric and stratospheric aerosols were improved. The land surface scheme ISBA (Interaction between Soil Biosphere and Atmosphere) (Noilhan and Planton1989; Noilhan and Mahfouf 1996) was externalized from the atmospheric model through the SURFEX (SURFface EXternalisée) platform and included new developments such as a parameterization of sub-grid hydrology (Decharme and Douville 2006, 2007), a new freezing scheme and a new bulk parameterization for ocean surface fluxes. These developments generally improve the simulation of present-day climate in terms of near surface temperature and large-scale circulation (Voldoire et al. 2013).

2.2 IPCC AR5 scenarios

For the IPCC AR5, four scenarios were designed: RCP 2.6, RCP 4.5, RCP 6.0 and RCP 8.5. All of these are considered likely changes in future anthropogenic greenhouse gas emissions, with a possible range of radiative forcing in the year 2100 relative to 1850 of 2.6, 4.5, 6.0, and 8.5 W m^{-2}, respectively. The RCP 2.6 is a mitigation scenario and the RCP 4.5 and RCP 6.0 represent stabilization scenarios, while the RCP 8.5 is a scenario of extremely high greenhouse gas emissions (IPCC 2013). The historical simulation forced by the observed atmospheric composition changes was integrated from 1850 to 2005. We extracted the simulation results over the recent 20 years from 1981 to 2000 to demonstrate present-day climate. The RCP 8.5

simulation was integrated from 2006 to 2100, and the outputs over the last 20 years from 2081 to 2100 were used to reflect future climate. The historical and RCP 8.5 simulations of CNRM-CM5 were compared to investigate the changes of BSISOs under the global warming context. The reason for choosing RCP 8.5 rather than RCP 4.5 or RCP 6.0 is that more pronounced changes are likely to be identified in this extreme warming scenario.

2.3 Validation data

To validate the simulation of the CNRM-CM5 model for the present-day climate, we compared the results of the CNRM-CM5 simulation with those of observational data in terms of seasonal-mean circulation and rainfall for the period 1981–2000. Monthly gridded rainfall and horizontal winds at 850-hPa were extracted from the Japanese 55-year Reanalysis project conducted by the Japan Meteorological Agency (Kobayashi et al. 2015). Both the precipitation and horizontal wind data have a horizontal resolution of 1.25° × 1.25°.

2.4 Methods

We first examined the changes of summertime (1 May to 31 October) seasonal-mean rainfall, 850-hPa winds, sea surface temperature (SST) and moisture at the planetary boundary layer (PBL; below 700-hPa), since these are seasonal-mean background closely related to BSISOs. Daily anomalies for key variables (such as rainfall and 850-hPa zonal winds) of BSISOs were obtained by removing the seasonal cycle (time-mean and the first three harmonics of the daily-resolved climatology) and interannual and decadal variability (the mean of the last 120 day) (Lee et al. 2013) for the twentieth and the twenty-first century simulations. A 10-day running mean was then applied to the anomaly time series for each variable to remove the high-frequency components not of interest here, thus isolating the intraseasonal signals (Li et al. 2015). Both rainfall and zonal winds at 850-hPa were used to represent the BSISO activities in the CNRM-CM5 model because the coupling between low-level atmospheric circulation and tropical convection is the major feature of BSISOs (Hsu and Weng 2001; Jiang et al. 2004). Although satellite-observed outgoing longwave radiation (OLR) is a good proxy for tropical convection (Liebmann and Smith 1996), the OLR in the CNRM-CM5 model is calculated from the temperature at the top of model clouds that have a number of uncertainties (Arakawa 2004). Therefore, the modeled OLR is not as good as the satellite-based OLR to represent tropical convective situation. Instead, the modeled rainfall is a commonly used variable to reflect the intraseasonal behaviors of tropical convection (Hung et al. 2013; Jiang et al. 2015), thus it is utilized to reveal the changes of BSISO activities.

Fig. 1 Regression coefficients (*shading*) of OLR anomalies against ▶ the **a** South Asian Dipole Index (SADI) and **b** East Asian Dipole Index (EADI) during the boreal summer (May–October) for the period 1981–2000. *Stippling* indicates the regions where the coefficients are statistically significant at the 5 % significance level. **c** Composite evolutions of OLR (*color scale*, W m^{-2}) and 850-hPa wind (*vectors*, m s^{-1}) anomalies based on the quadrupole pattern index (QPI) during a BSISO cycle for phases 1–8. Only shown are the OLR and wind anomalies that are statistically significant at the 5 % significance level. The magnitude of the reference vector is provided at the *bottom right*. The *four rectangular areas* denote the key regions used for calculating the SADI and EADI

Wavenumber-frequency spectra of rainfall and 850-hPa zonal wind intraseasonal anomalies under different climate conditions were compared to study the changes in amplitude and frequency of the equatorial eastward propagation. We also used the longitude–lag–time correlation diagram, in which anomalies of the associated variables at each grid point were regressed at the different time lags against the reference time series to confirm the changes of eastward propagation along the equator. The statistical significance for regression or correlation coefficients was tested on the basis of two-tailed probabilities.

Lee et al. (2013) conducted the multivariate empirical orthogonal function (MV-EOF) of OLR and 850-hPa zonal wind anomalies over the ASM region and used the first and second principal components of MV-EOF to represent the evolution of the 30–60-day BSISO in the form of the characteristic quadrupole pattern of convection anomalies. Given that the quadrupole pattern actually consists of the SASM dipole and the complementary EA/WNP dipole, which are connected by the equatorial eastward-propagating component (Annamalai and Slingo 2001; Annamalai and Sperber 2005), we proposed an alternative method to represent this quadrupole pattern and its evolution: first, the South Asian Dipole Index (SADI) and East Asian Dipole Index (EADI) were constructed, respectively; then, the quadrupole pattern index (QPI) was defined as the difference between the SADI and EADI, so as to represent the complementary phase relationship between two dipoles over the SASM and EA/WNP areas.

Because the meridional dipole pattern along the Indian longitudes is actually a time–lagged dipole pattern, with the wettest convection anomalies over the EIO lagging the driest convection anomalies around 15°N by about 10 days, the SADI was defined in the following procedure: (1) lead-lag correlation coefficients between the area-averaged 30–60-day filtered OLR anomalies over the EIO and the Arabian Sea–Indian subcontinent–BOB (10°–25°N, 70°–100°E) were calculated, and (2) the SADI at a particular time t was defined as the difference between the 30–60-day filtered OLR anomalies over the EIO at time $(t + t_{lag})$ and

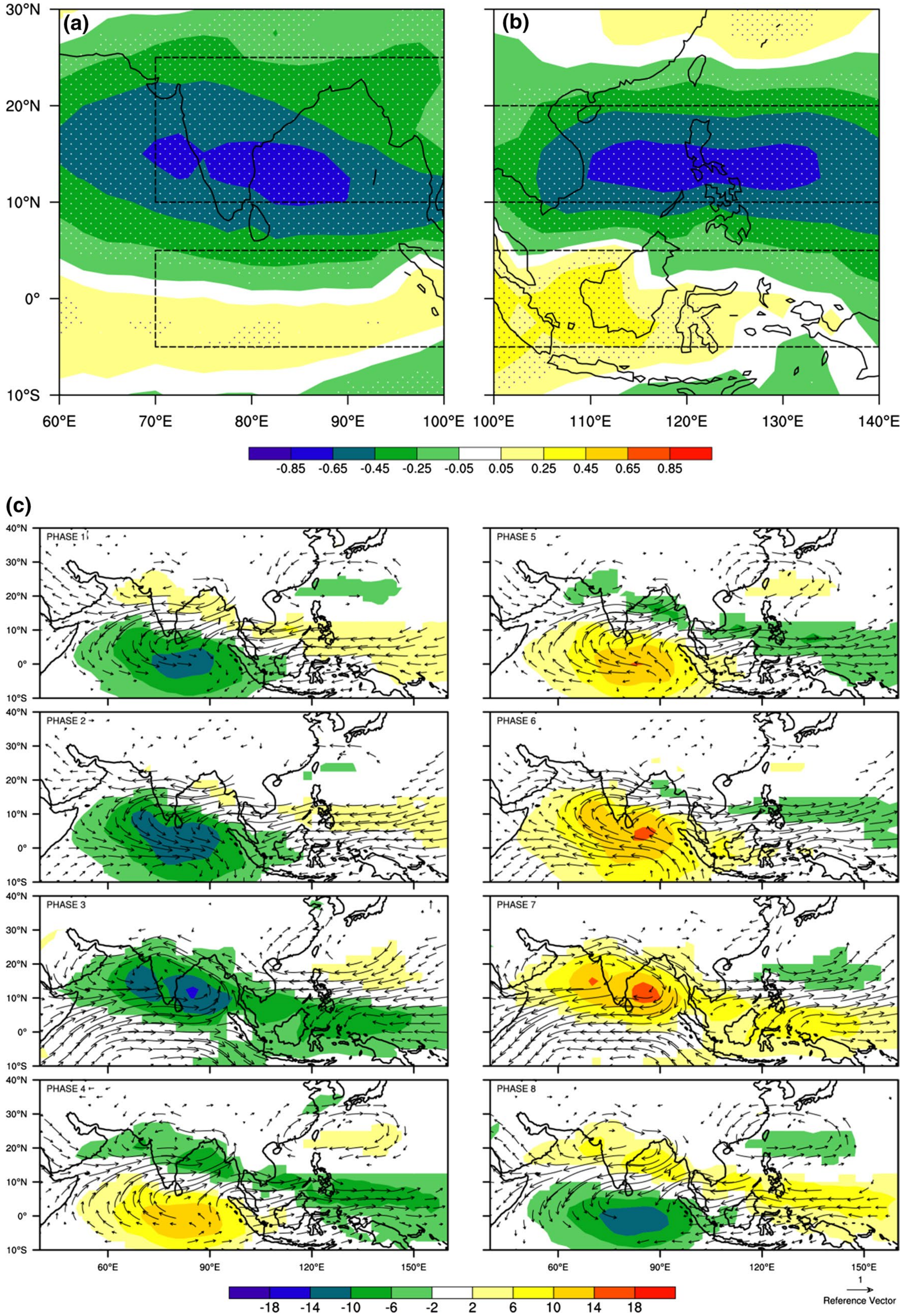
(a)
(b)
30°N
20°N
10°N
0°
10°S
60°E
70°E
80°E
90°E
100°E
100°E
110°E
120°E
130°E
140°E
-0.85 -0.65 -0.45 -0.25 -0.05 0.05 0.25 0.45 0.65 0.85
(c)
PHASE 1
PHASE 2
PHASE 3
PHASE 4
PHASE 5
PHASE 6
PHASE 7
PHASE 8
40°N
30°N
20°N
10°N
0°
10°S
60°E
90°E
120°E
150°E
-18 -14 -10 -6 -2 2 6 10 14 18
1
Reference Vector

the 30–60-day filtered OLR anomalies over the Arabian Sea–Indian subcontinent–BOB at the time *t*, with t_{lag} being the lag at which the negative correlation coefficient peaks. Figure 1a displays the regression coefficients of the 30–60-day filtered OLR regressed against the SADI. The regression coefficients exhibit a seesaw pattern between the EIO and Arabian Sea–Indian subcontinent–BOB, indicating that the above-defined SADI sufficiently represents the northward propagation over the SASM region.

The northward/northwestward propagation over the EA/WNP area also gives rise to the lagged dipole pattern within the western Pacific longitudes, with the convection anomalies over the EWP lagging those of the opposite sign over the WNP by 10 days. Therefore, we similarly defined the EADI at time *t* as the difference between the area-averaged 30–60-day filtered OLR anomalies over the EWP at time ($t + t_{lag}$) and the area-averaged 30–60-day filtered OLR anomalies over the WNP at the time *t*, with t_{lag} being the lag at which the correlation coefficient reaches the minimum. The spatial distribution of regression coefficients against the EADI also supports the definition of EADI (Fig. 1b).

To test the feasibility of QPI, composites of OLR and 850-hPa wind anomalies were made during phases 1–8 of standardized QPI (Fig. 1c). Phase 1 represents the transition of QPI from negative to positive, while phase 3 represents the maximum of QPI. Phase 5 is the transition from positive to negative QPI, while phase 7 indicates the minimum of QPI. Phase 2 and phase 4 (phase 6 and phase 8) occur at times when QPI reaches 0.5 standard deviation above (below) zero. As shown in Fig. 1c, the structure and evolution of the 30–60-day BSISO reflected by QPI are similar to those in Lee et al. (2013), see fig. 9 in that study), confirming that the definition of QPI is reasonable.

Although the CNRM-CM5 model reproduces the northward propagations over both the SASM and EA/WNP areas, the complementary relationship between these two dipoles is not well captured, with the SASM dipole being accompanied by convection anomalies with the same sign over the EWP and SCS (see fig. 11k of Sabeerali et al. 2013). Therefore, changes of northward propagation over the SASM and EA/WNP regions were analyzed separately in the present study. As mentioned above, the modeled rainfall is better at reflecting tropical convection than modeled OLR, the SADI and EADI of the CNRM-CM5 simulation were defined using modeled rainfall instead of OLR. Based on the standardized SADI (EADI), northward propagation of the BSISO over the SASM (EA/WNP) area was also divided into eight phases. Composite analyses for the rainfall-associated variables (such as vertical motions and moisture) were made according to the above phase classification to further examine the changes of northward propagation characteristics of the BSISO and to explore the mechanisms behind the modifications. The statistical significance for composite fields of anomalous variables was estimated based on Student's *t* test. Note that in testing the statistical significance of composite anomalies as well as regression or correlation coefficients, the effective sample size of the intraseasonal time series for a particular variable was recalculated using the method of Bretherton et al. (1990), since the time filtering could reduce the degree of freedom of the filtered time series.

3 Changes in boreal summer climate

Reasonable simulations of BSISOs depend on a well-reproduced summertime seasonal-mean state (e.g., Sperber and Annamalai 2008). Figure 2 compares the distributions of climatological summer rainfall and 850-hPa winds derived from the reanalysis data and the simulation results to show how well the CNRM-CM5 model reproduces the seasonal-mean background. During the boreal summer, as shown in Fig. 2a, the belts of subtropical high break into anticyclone centers in both hemispheres. The northeasterlies on the southern side of the subtropical anticyclone in the Northern Hemisphere and the southeasterlies on the northern side of the subtropical anticyclone in the Southern Hemisphere converge toward the equator, leading to the inter-tropical convergence zones (ITCZ) over the Pacific and Atlantic Oceans. Strong Somali cross-equatorial flows that originate from the Mascarene anticyclone in the Southern Hemisphere veer toward the east on the north side of the equator, forming a low-level westerly jet from the Arabian Sea to the BOB and a large-scale cyclonic vorticity extending from the northern BOB to the EIO. This low-level circulation over the SASM region leads to a rainfall center (>8 mm day^{-1}) from the northern BOB to the eastern EIO. Over the EA/WNP sector, there is a distinct northeast-southwest oriented extratropical rain-belt along the East Asian coast, which is associated with the subtropical EASM. This extratropical rain-belt is separated by the WNP subtropical anticyclone from the tropical rain-belt, in a band stretching from the SCS into the EWP, which results from the monsoon trough. The tropical rain-belt is also related to cross-equatorial flows from Australia and upstream westerlies from the northern Indian Ocean. The extratropical rain-belt is caused by the Meiyu (in China)-Baiu (in Japan)-Changma (in Korea) front, in association with the southwesterlies on the northwestern side of the WNP subtropical anticyclone.

Compared with Fig. 2a, the CNRM-CM5 model sufficiently captures the present-day climate during the boreal summer, reproducing all the rain-belts and main circulation

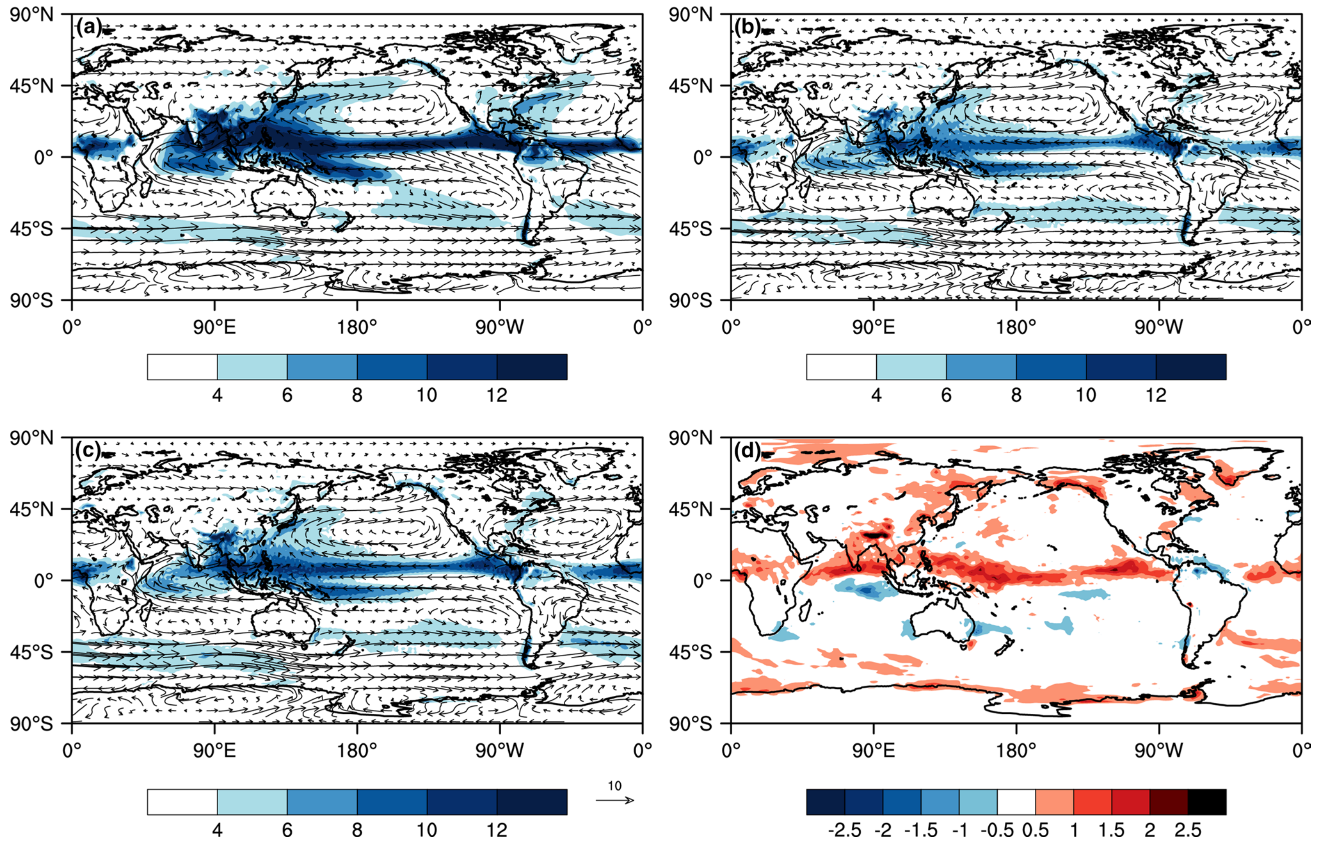

Fig. 2 Distributions of climatological summer (1 May to 31 October) rainfall (*color scale*, mm day^{-1}) and 850-hPa winds (*vectors*, m s^{-1}) in the twentieth century derived from **a** JRA-55 reanalysis data for the period 1981–2000, **b** historical simulations for the period 1981–2000, and **c** in the twenty-first century derived from global warming simulations for the period 2081–2100. The magnitude of the reference vector is provided at the *bottom right*. **d** The differences (*color scale*, mm day^{-1}) of simulated climatological summer rainfall between **c** the twenty-first century and **b** the twentieth century

systems, especially over the ASM region (Fig. 2b), although the simulated rainfall over the EIO is weaker and extends more westward to near the eastern African coast. The global pattern correlation between observed and simulated rainfall reaches 0.87, consistent with the result of Sabeerali et al. (2013). Note the underestimation of simulated rainfall over global tropical and subtropical zones in the Northern Hemisphere, while rainfall over mid-latitudes in the Southern Hemisphere is overestimated. This implies that the CNRM-CM5 model may underestimate rainfall over the ASM area. Also overestimated is the rainfall in the tropical Pacific south of the equator, which is associated with the so-called double ITCZ (Lin et al. 2006; Voldoire et al. 2013).

In the global warming scenario, while the spatial pattern of large-scale circulations is similar to that in the twentieth century (Fig. 2c), the rainfall over the northern Indian Ocean, including the Indian and Indochina peninsulas, and the ITCZs in the tropical Pacific and the tropical eastern Atlantic increase significantly. This can be identified more clearly by the differences in summertime seasonal-mean rainfall between the twenty-first and the twentieth century (Fig. 2d), with an increase being on the order of 1.5 mm day^{-1}. The increase of rainfall over both the Arabian Sea and the equatorial eastern Pacific implies that tropical convection will take place in a broader region in the twenty-first century. Note that the rainfall over the EIO south of the equator is decreased unexpectedly. A similar phenomenon is also derived from other models such as CCSM4 under the identical global warming scenario, as shown in Subramanian et al. (2014).

Based on a moist static energy budget analysis, Neelin and Held (1987) stated that tropical convection centers generally correspond with the oceanic areas of higher SSTs. The warmer ocean can transport more water vapor into the lower atmosphere, increasing the moist static energy, thus favoring occurrence of deep convection. As a consequence, under the warmed climate condition, the intensified rainbelt is likely to result from the changes of SSTs and resultant increased moisture in the lower atmosphere. Therefore, Fig. 3 displays the seasonal-mean SST and PBL saturation specific humidity during summertime in the historical and

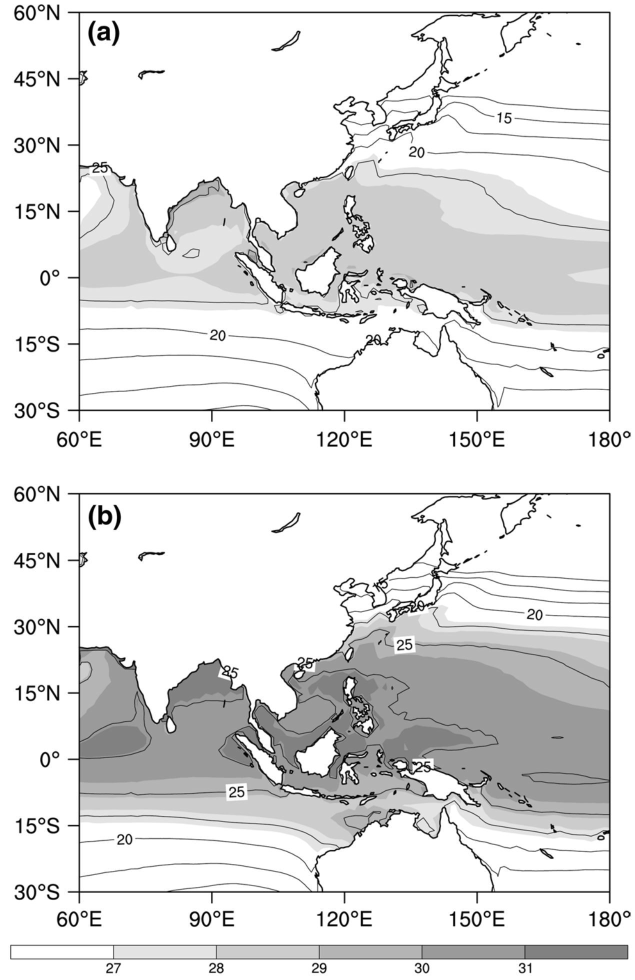

Fig. 3 Distributions of climatological sea surface temperatures (*shading*, °C) and 1000-hPa saturation specific humidity (*contours*, g kg^{-1}; contour interval is 2.5 g kg^{-1}) during the boreal summer (1 May to 31 October) in **a** the twentieth century for the period 1981–2000 and **b** the twenty-first century for the period 2081–2100

RCP 8.5 runs. For the present-day climate simulation, the Indo-Pacific warm pool (enclosed by the 28 °C isotherm), which is closely related to the rain-belt from the BOB through the SCS to the tropical WNP, is well simulated (Fig. 3a), indicating that the close connection between rainfall and SST is reasonably reproduced in the CNRM-CM5 model.

In the extreme warming scenario, both the tropical and subtropical Indian Ocean–western Pacific get warmer significantly, with SSTs in the entire northern Indian Ocean and western North Pacific rising universally from 28 °C in the twentieth century to 30 °C (Fig. 3b). As a result, the actual Indo-Pacific warm pool covers a much larger area as compared with the present-day situation. Note that several higher SST centers above 31 °C exist in the Arabian Sea, the northern BOB, and the SCS where the ASM monsoon prevails. Because the warm pool serves as an important source of moisture for the atmosphere, it is conceivable that the future changes in tropical SSTs may affect the hydrological cycle. Based on the Clausius–Clapeyron equation for the atmospheric water vapor, the warmed SSTs indicate a new equilibrium between the ocean and atmosphere, with the saturation specific humidity increasing by about 7 % for each 1 °C warming in SSTs (Held and Soden 2006). As the Indo-Pacific warm pool gets warmer by around 2.5 °C, the area-averaged saturation specific humidity in the near sea surface atmosphere over the warm pool may increase by about 16 % (Fig. 3b). Because the saturation specific humidity denotes the water-holding capacity of the atmosphere, the increased saturation vapor pressure of the near sea surface atmosphere over the warm pool will enhance the upward latent heat fluxes, transporting more moisture into the lower-level atmosphere, thus providing a favorable condition for rainfall occurrence. Note that over the EIO, the mean rainfall will tend to decrease (Fig. 2d) in the future, even though the local SST increases (Fig. 3b). This may be attributed to the decreased vertical velocity at 500-hPa over the EIO in the warmer climate (Subramanian et al. 2014). Why the atmospheric response over the EIO differs from that over other oceanic areas needs further investigation.

Because seasonal-mean and intraseasonal variations share the same spatial modes of variability (Molteni et al. 2003), the significant modifications of seasonal-mean background by global warming implies that intraseasonal oscillations may also behave differently in the warmed climate. Liu (2013) and Subramanian et al. (2014) pointed out that in response to the increase of low-level water vapor, MJO activities are enhanced significantly by global warming. Thus, the moister lower troposphere may lead to modifications of convection activities on the intraseasonal timescale. Will the amplitude of BSISOs also intensify under global warming? Will there be changes of periodicity and propagating patterns of the BSISOs? These questions are addressed in the next section.

4 Changes in the BSISOs

4.1 Changes in the spatial distribution and amplitude of BSISOs

Figure 4a presents the simulated standard deviations of BSISOs in the present-day climate. Consistent with the observations (see fig. 1b in Lee et al. 2013), most BSISO activities are reproduced over the EIO, the BOB and the SCS–tropical WNP (Fig. 4a), although the strength of intraseasonal rainfall anomalies over these centers is underestimated. The twentieth-century simulation also properly represents the spatial distribution of 850-hPa zonal wind

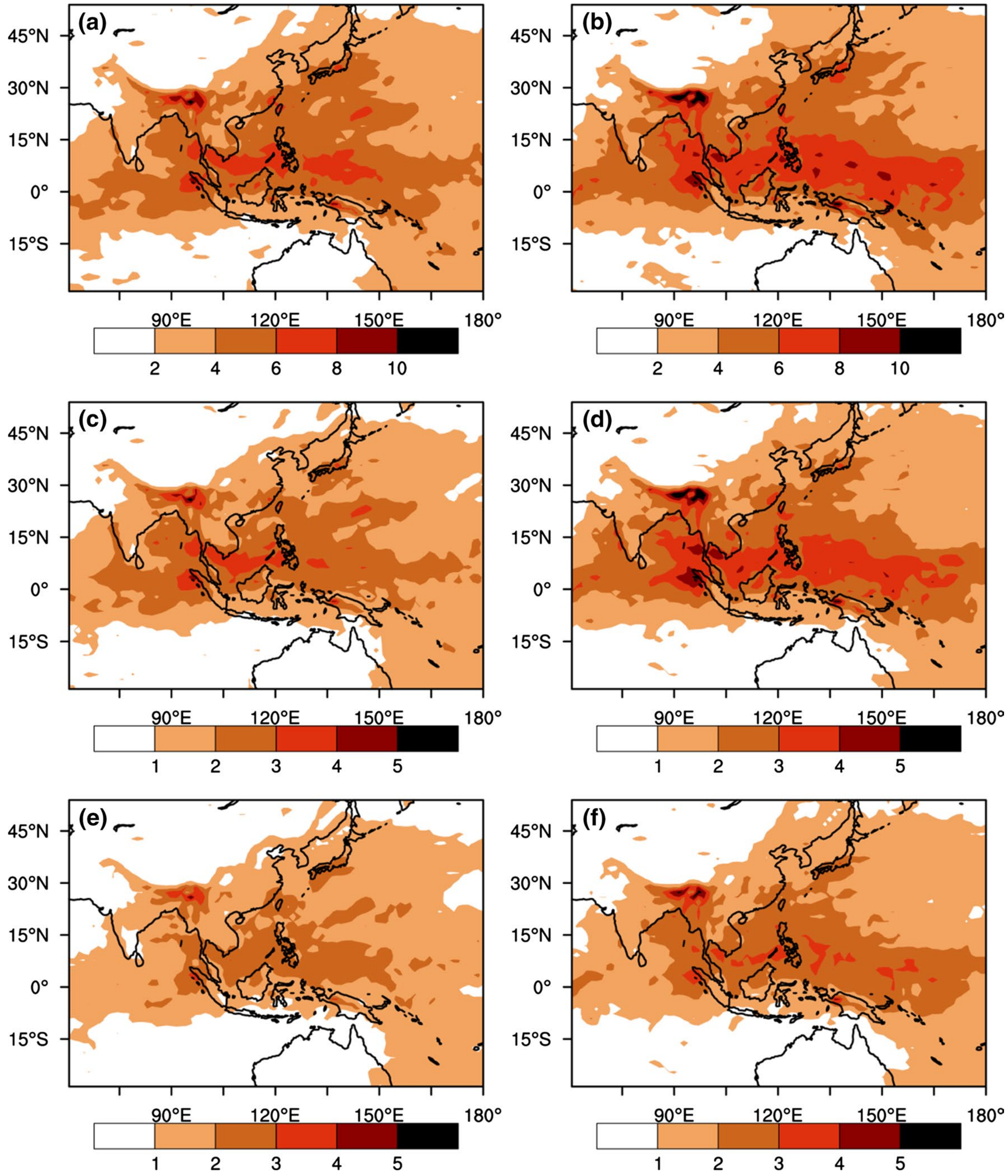

Fig. 4 Standard deviations of the **a** unfiltered, **c** 30–60-day filtered and **e** 10–20-day filtered intraseasonal rainfall anomalies (*color scale*, mm day^{-1}) during the boreal summer (1 May to 31 October) derived from the twentieth century simulation for the period 1981–2000. **b**, **d**, **f** As in (**a**), (**c**) and (**e**) except for the twenty-first century simulation for the period 2081–2100

anomalies on the intraseasonal timescale (not shown), with a high pattern correlation (0.89) with the observations. These indicate that the CNRM-CM5 model provides a reasonable representation of the intraseasonal coupled circulation–convection systems over the entire ASM region during the boreal summer. In the extreme warming scenario, amplitudes of BSISOs over the eastern EIO, the BOB as well as the tropical western Pacific increase significantly (Fig. 4b), in agreement with the results of Sabeerali et al. (2014). Moreover, the BSISO activities are confined mostly to the west of 150°E in the present-day simulation (Fig. 4a) due to water vapor deficiency over the tropical central-eastern Pacific, while the future warmer and wetter PBL will promote the BSISO activities more eastward, with the isoline of 8 mm day^{-1} extending to around the dateline (Fig. 4b).

The BSISO activities over the ASM are mainly made up of 30–60-day and 10–20-day modes. How and to what extent does each of these two dominant modes change in the warming scenario? As shown in Fig. 4c, e, both 30–60-day and 10–20-day oscillations share the same spatial distribution with total BSISO activity. However, amplitudes of major activity centers of the 30–60-day BSISO are much larger than those of the 10–20-day BSISO. This is consistent with the observation that the 30–60-day BSISO explained about 67 % of the overall intraseasonal variability over the ASM area (Annamalai and Slingo 2001), implying that the CNRM-CM5 model again captures the intraseasonal feature that the 30–60-day BSISO predominates over the 10–20-day mode.

In the twenty-first century, the intensities of 30–60-day rainfall anomalies will increase significantly over the eastern EIO and the BOB as well as the tropical western Pacific under the RCP8.5 scenario (Fig. 4d), with the isoline of 3 mm day^{-1} covering a larger area. In contrast, intensifications of 10–20-day BSISO (about 0.5 mm day^{-1}) are not significant compared with the 30–60-day mode (1–2 mm day^{-1}) (Fig. 4d, f), indicating that the intensified BSISO activities under global warming are contributed more by the 30–60-day mode. Therefore, in the following subsections, we mainly examine the possible changes of the 30–60-day BSISO over the ASM in a warmer climate.

4.2 Changes in the equatorial eastward propagation

The evolution of the 30–60-day BSISO over the ASM region comprises three components: the equatorial eastward propagation, northward propagation over the SASM and northwestward/northward propagation over the EA/WNP regions (Annamalai and Slingo 2001; Lee et al. 2013). As the meridional propagation components are considered as Rossby wave responses to the equatorial eastward propagation modulated by the seasonal-mean monsoon circulation (Wang and Xie 1997; Annamalai and Sperber 2005), the change of the equatorial eastward propagation is crucial for the life cycle of 30–60-day BSISO activities over the ASM area.

Frequency-wavenumber power spectra of equatorial intraseasonal rainfall and 850-hPa zonal wind anomalies (Fig. 5a) show that the CNRM-CM5 model successfully reproduces the equatorial eastward propagation, with the spectral peaks concentrating at zonal wavenumbers 1–2 and a frequency band of 0.016–0.033 cycle per day (equivalent to a period of 30–60 days). There is also a westward propagating component in the 850-hPa zonal winds, with a period of 30–60 days, but the amplitude is much weaker than its eastward counterpart. Under the global warming scenario, power spectra in both equatorial rainfall and 850-hPa zonal wind anomalies are increased evidently within a broader frequency band of 0.01–0.033 cycle per day (equivalent to the period of 30–100 days) and zonal wavenumbers

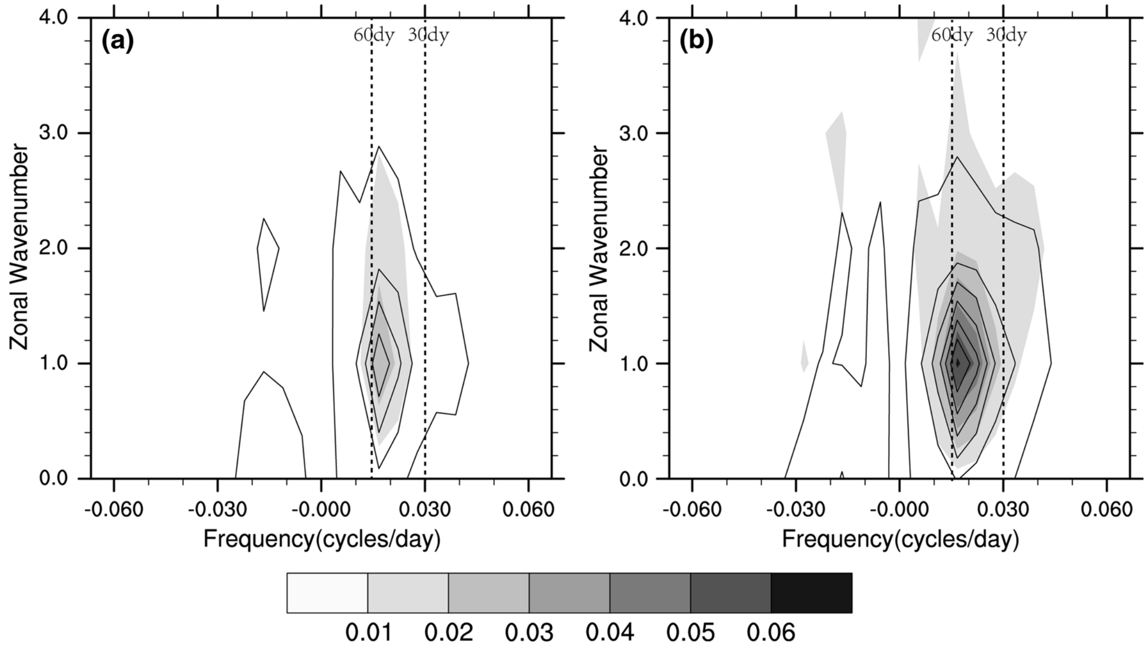

Fig. 5 Wavenumber-frequency power spectra of the boreal summer (1 May to 31 October) equatorial (10°S–25°N) intraseasonal rainfall (*shading*, mm^2 day^{-2}) and 850-hPa zonal wind (*contours*, m^2 s^{-2}; the contours start from 0.01 with an interval of 0.03) anomalies for **a** the twentieth century and **b** the twenty-first century simulations. The periods used to calculate are the last twenty years from each century

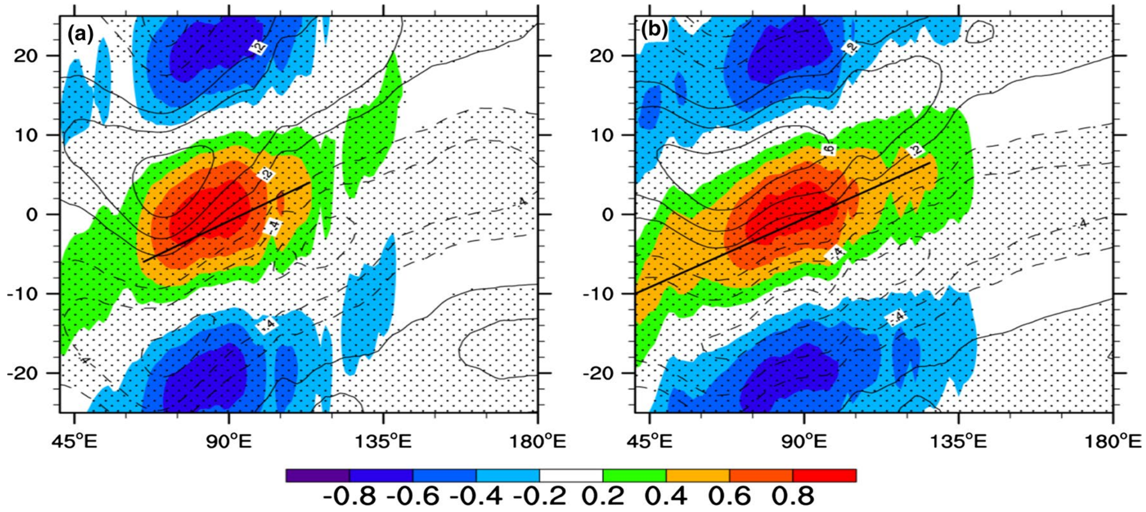

Fig. 6 Lagged–time–longitude diagram of correlation coefficients between 30 and 60-day band-pass filtered rainfall (*color scale*) and 850-hPa zonal wind (*contours*) anomalies over the equatorial regions (10°S–10°N) against area-averaged 30–60-day filtered rainfall over the EIO (10°S–5°N, 75°–100°E) for the boreal summer (1 May to 31 October) for **a** the twentieth century simulation computed from the period 1981–2000 and **b** the twenty-first century simulation calculated from the period 2081–2100. The contour interval is 0.1, with the *zero contour omitted* and *negative contours dashed*. The *stippling* indicates the regions where both correlation coefficients are statistically significant at the 5 % significance level. *Thickened solid lines* indicate the equatorial eastward propagation

1–2 (increased by 0.12 $mm^2\ day^{-2}$ and 0.25 $m^2\ s^{-2}$, respectively) (Fig. 5b), indicating a strengthening of the intraseasonal coupled circulation–convection system. Note that the increases of power spectra occur mostly in the frequency band corresponding to 30–60 days, with increased spectra within the 30–60-day frequency band being about 0.098 $mm^2\ day^{-2}$ (0.2 $m^2\ s^{-2}$) for intraseasonal rainfall (850-hPa zonal wind), accounting for 81.6 % (80 %) of the totally increased spectra of 0.12 $mm^2\ day^{-2}$ (0.25 $m^2\ s^{-2}$) in the entire (30–100-day) frequency band. Since the spectral peak concentrates within the 30–60-day frequency band in the present-day climate and since the maximum spectral increase again appears within the 30–60-day frequency band in the global warming scenario, it is implied that the phase speed of the equatorial eastward propagation will not change significantly in the warmed climate.

To further confirm the changes of the fundamental propagating and time-varying nature of the equatorial component, Fig. 6 presents the time–lag–longitude diagrams of simulated 30–60-day rainfall and 850-hPa zonal wind regressed against the area-averaged rainfall over the EIO. The evident eastward propagation across the Eastern Hemisphere is reproduced well in the historical simulation (Fig. 6a), with strong signals originating from the central Indian Ocean and then moving eastward across the Maritime Continent and quickly decaying beyond the 120°E. The eastward phase speed is about 7.4 $m\ s^{-1}$, with the positive rainfall anomaly leading the anomalous westerly by 4–5 days. In the RCP 8.5 run, the origin of the equatorial eastward propagation extends westward to the western Indian Ocean. Moreover, strong rainfall anomalies propagate more eastward to 135°–140°E in the RCP 8.5 run (Fig. 6b). Consistent with Fig. 4d, the BSISO activities are observed in a broader area along the equator under the warmer climate. Note that the phase speed is about 7.26 $m\ s^{-1}$, also implying that the phase speed of the equatorial eastward propagation will remain almost unchanged in the global warming scenario. It has been stated in Sect. 3 that the warmer SSTs of the Indo-Pacific warm pool lead to a wetter PBL (Fig. 3b), with a significant increase in moisture-holding capacity. This increase in the residence time of atmospheric moisture delays the triggering of convection, and thus tropical convections have more time to accumulate energy (Trenberth 2011). Therefore, the equatorial BSISOs intensify significantly.

4.3 Changes in the northward propagation over the SASM region

Lawrence and Webster (2002) suggested that the northward propagating BSISO over Indian longitudes occurs mostly in conjunction with the equatorial eastward propagating component. The diagnostic results in Sect. 4.2 indicate a stronger eastward movement along the equator in the global warming scenario. We will further examine the changes of the associated poleward propagation in the warmer climate.

As the 30–60-day BSISO over the Indian Ocean longitudes is confined mainly to latitudinal zone between 10°S and 30°N, it is assumed that the BSISO activities nearly vanish around the most southern and northern latitudes

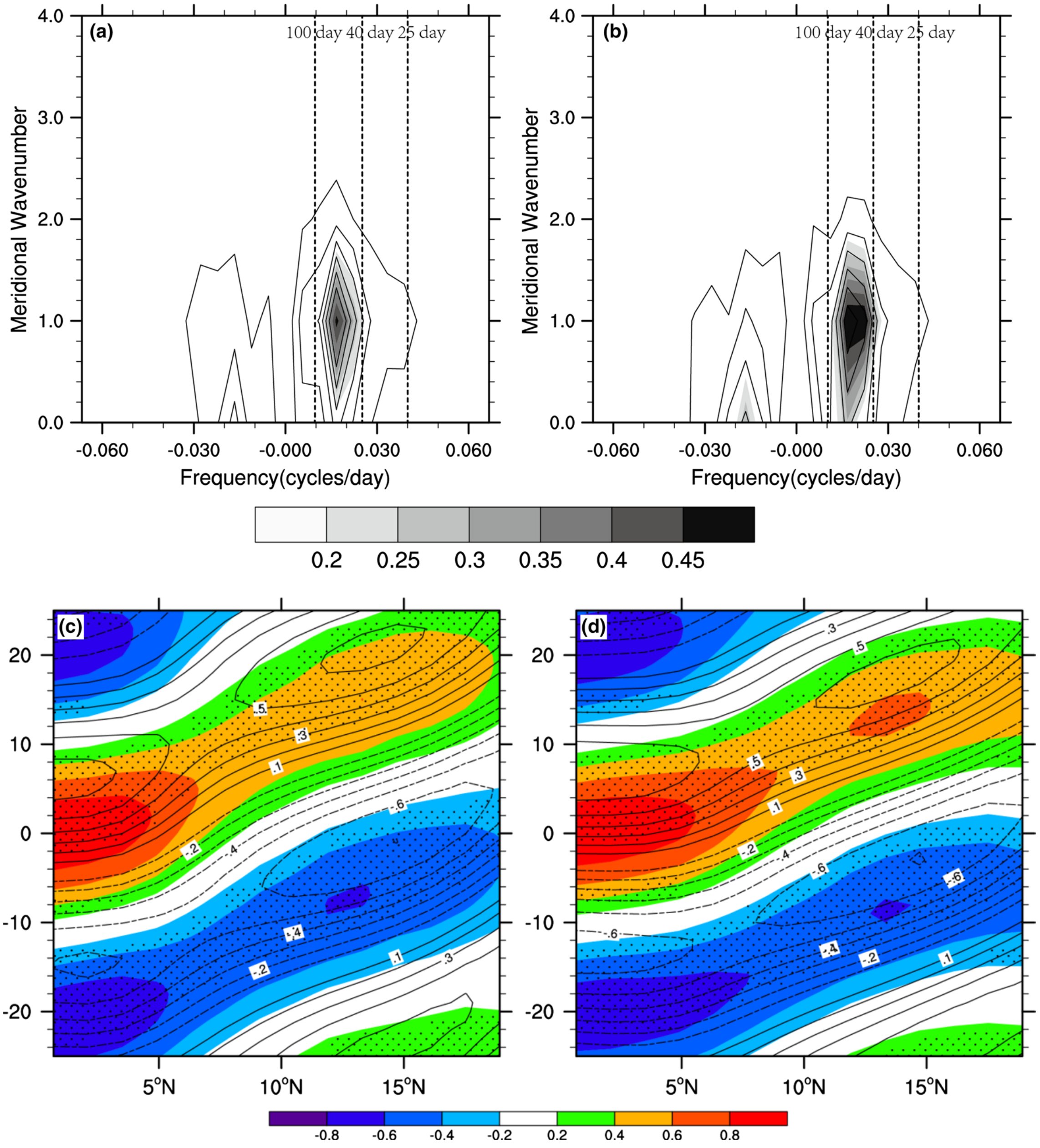

Fig. 7 Finite domain wavenumber-frequency power spectra of the boreal summer (1 May to 31 October) intraseasonal rainfall (*shading*, mm^2 day^{-2}) and 850-hPa zonal wind (*contour*, m^2 s^{-2}, the contours start from 0.05 with an interval of 0.05) calculated over the SASM area (10°S–30°N, 70°–100°E) for **a** the twentieth century and **b** the twenty-first century simulations. The period used to calculate is the last 20 years from each century. Lagged–time–latitude diagram of correlation coefficients between 30 and 60-day band-pass filtered rainfall (*color scale*) and 850-hPa zonal wind (*contours*) anomalies over the Indian Ocean longitudes (70°–100°E) against the area-averaged 30–60-day filtered rainfall over the EIO (5°S–5°N, 70°–100°E) for **c** the twentieth century and **d** the twenty-first century simulations. The contour interval is 0.1, with the *zero contour omitted* and *negative contours dashed*. The *stippling* indicates the regions where both correlation coefficients are statistically significant at the 5 % significance level

of this zone, thus we conduct finite domain wavenumber-frequency analysis in the meridional direction. Because the series of intraseasonal rainfall or 850-hPa zonal wind in the meridional direction is not cyclic, a split-cosine-bell tapering is applied before the Fourier transform to reduce the leakage from spectral peaks, with 10 % of the series tapered (Teng and Wang 2003). In the present-day climate, the maximum spectra are found in meridional number 1 at the northward propagating direction (Fig. 7a). Note that the meridional number here indicates the spatial scales within the above mentioned latitudinal domain. Therefore, the maximum spectra in meridional number 1 indicate that the BSISO activities over the EIO are always out of phase with those over the Indian Subcontinent. The latitude–time diagram further confirms the poleward propagation from the equator to 20°N along the Indian longitudes (Fig. 7c), with anomalous rainfall leading the zonal wind anomalies by 6 days. This phase relationship between the zonal wind and rainfall anomalies is similar to the analytical solution of heat-induced tropical circulation for asymmetric heating around the equator (Gill 1980).

In the twenty-first century, the amplitudes of both rainfall and zonal wind anomalies intensify in the northward propagation, with the power spectra of intraseasonal rainfall (850 hPa zonal wind) within the frequency band of 0.01–0.04 cycle per day (equivalent to 25–100 days) and meridional numbers 1–2 increasing by 38.6 % (11 %) relative to the present-day climate. The lagged–time–latitude diagram also shows that the northward-propagating coupled convection–circulation system strengthens in the global warming scenario, especially between 10°N and 15°N (Fig. 7b, d). Note that the power spectra of intraseasonal rainfall are increased by 0.52 $mm^2\ day^{-2}$ within the 0.01–0.025 frequency band (equivalent to the period of 40–100-day), but the increased magnitude of the spectra within the 0.025–0.04 frequency band (equivalent to the period of 25–40-day) is only 0.26 $mm^2\ day^{-2}$. The power spectra of intraseasonal 850-hPa zonal wind are also increased more evidently within the 0.01–0.025 frequency band. These indicate that the relatively slower components propagating northward will enhance more significantly. Such different increases of power spectra from different frequency components of the BSISO imply that the phase speed of the northward propagation possibly becomes slower under the global warming scenario. Similar results were revealed by Sabeerali et al. (2014), who studied the changes of the meridional propagation of BSISOs over the Indian Ocean. Note also that the same phase relationship of the 30–60-day convection–circulation system exists in the global warming scenario, with positive rainfall anomalies still leading the anomalous 850-hPa westerlies by 5–6 days in the northward propagation, indicating that the climate change hardly modifies the mechanism for northward propagation.

Due to the northward propagation, the 30–60-day convection anomalies exhibit a lagged south-north oriented seesaw pattern along the Indian longitudes (e.g., Annamalai and Slingo 2001), with the active convection anomalies over the EIO peaking 10 days after the northern pole (10°–25°N) reaches its driest phase. In the historical simulation, negative correlation coefficients between the two poles reach their maximum absolute value at the time when the northern pole leads the southern one by 7 days (Fig. 8), implying that the CNRM-CM5 model is to some extent capable of representing the dipole pattern in convection anomalies over the SASM region. Because the time lag of maximum negative correlation is determined by the northward propagation speed, the shorter time lag in the historical simulation compared with the observations indicates that the model has overestimated the northward propagation speed. Under global warming conditions, the negative correlation between these two poles reaches the maximum at a time lag of 9 days. This prolonged time lag suggests that the 30–60-day BSISO will move poleward more slowly in the future.

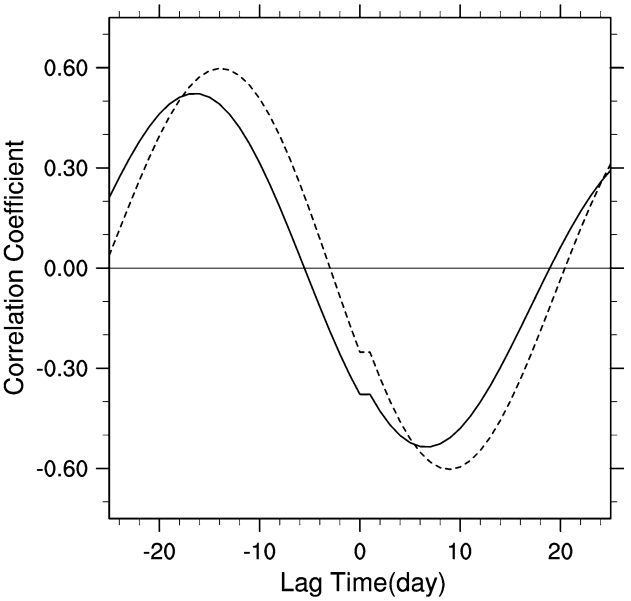

Fig. 8 Lead-lag correlation coefficients between the area-averaged rainfall anomalies over the EIO (5°S–5°N, 70°–100°E) and over the Arabian Sea–Indian Subcontinent–BOB (10°–25°N, 70°–100°E) in the twentieth century simulation (*solid line*) computed for the period from 1 May 1981 to 31 October 2000, and in the twenty-first century simulation (*dashed line*) computed for the period from 1 May 2081 to 31 October 2100

Based on the time–lag relation of CNRM-CM5 simulated rainfall, we similarly defined the model SADI. The significant regression coefficients of rainfall anomalies against the model SADI exhibit a distinct north–south oriented dipole over the SASM area (Fig. 9a, c), indicating that CNRM-CM5 well captures the northward propagation of the 30–60-day BSISO. Therefore, composite evolutions of rainfall and 850-hPa wind anomalies based on SADI were made to further investigate the reasons for the above changes in amplitude and phase speed of northward propagation along the Indian longitudes.

In the present-day climate (Fig. 10a), active convection anomaly accompanied by strong zonal wind convergence originates from the EIO in phase 3 and then moves eastward to the eastern Indian Ocean along the equator in phases 4–5. From phase 6, active convection anomalies start to extend poleward, with a cyclonic circulation

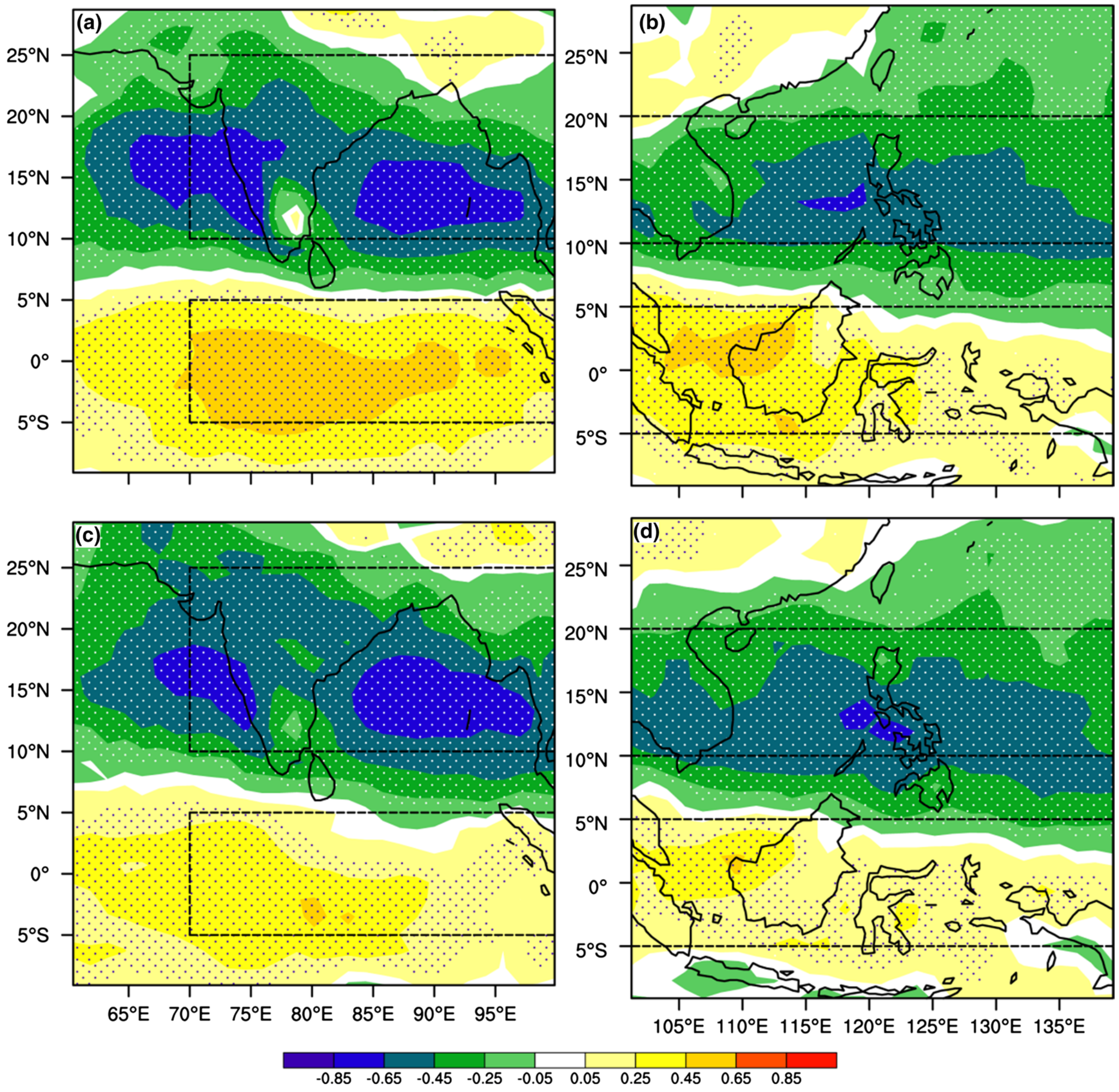

Fig. 9 Regression coefficients (*shading*) of rainfall anomalies against **a** the SADI and **b** the EADI during the boreal summer (1 May to 31 October) from the twentieth-century simulations. **c**, **d** As in (**a**) and (**b**) except for the twenty-first century simulations. *Stippling* indicates the regions where the regression coefficients are statistically significant at the 5 % significance level. The *two rectangles* represent the domains over which the time series of area-averaged intraseasonal rainfall anomaly are produced to calculate the SADI and EADI

to the northwest. Subsequently, active convection peaks over the Indian subcontinent and the BOB, with a huge cyclone occupying the area between 15°N and 20°N in phase 7. Meanwhile, a newly developed suppressed convection occurs over the EIO. While the active convection anomalies over the Indian Subcontinent and the BOB rapidly decay in phases 8 and 1, the suppressed convection anomalies propagate eastward and strengthen significantly, preparing for the northward propagation of the suppressed convection in phases 2–3. The above evolution again suggests that the northward propagation over the SASM is closely associated with the equatorial eastward-propagating signal.

In the RCP 8.5 scenario (Fig. 10b), the equatorial active convection originates from the western Indian Ocean in phase 3, also implying that the equatorial signal extends more westward under the global warming condition (Fig. 5b). This equatorial active convection then develops significantly while moving eastward to the eastern Indian Ocean in phases 4–5. Note that the equatorial signals in the RCP 8.5 run are much stronger than those in the present-day simulation. This stronger equatorial convection begins to propagate northward in phase 6, leading to the northwestern Indian subcontinent and the BOB being occupied by stronger active convection in phase 7. The above comparison again suggests that the intensification

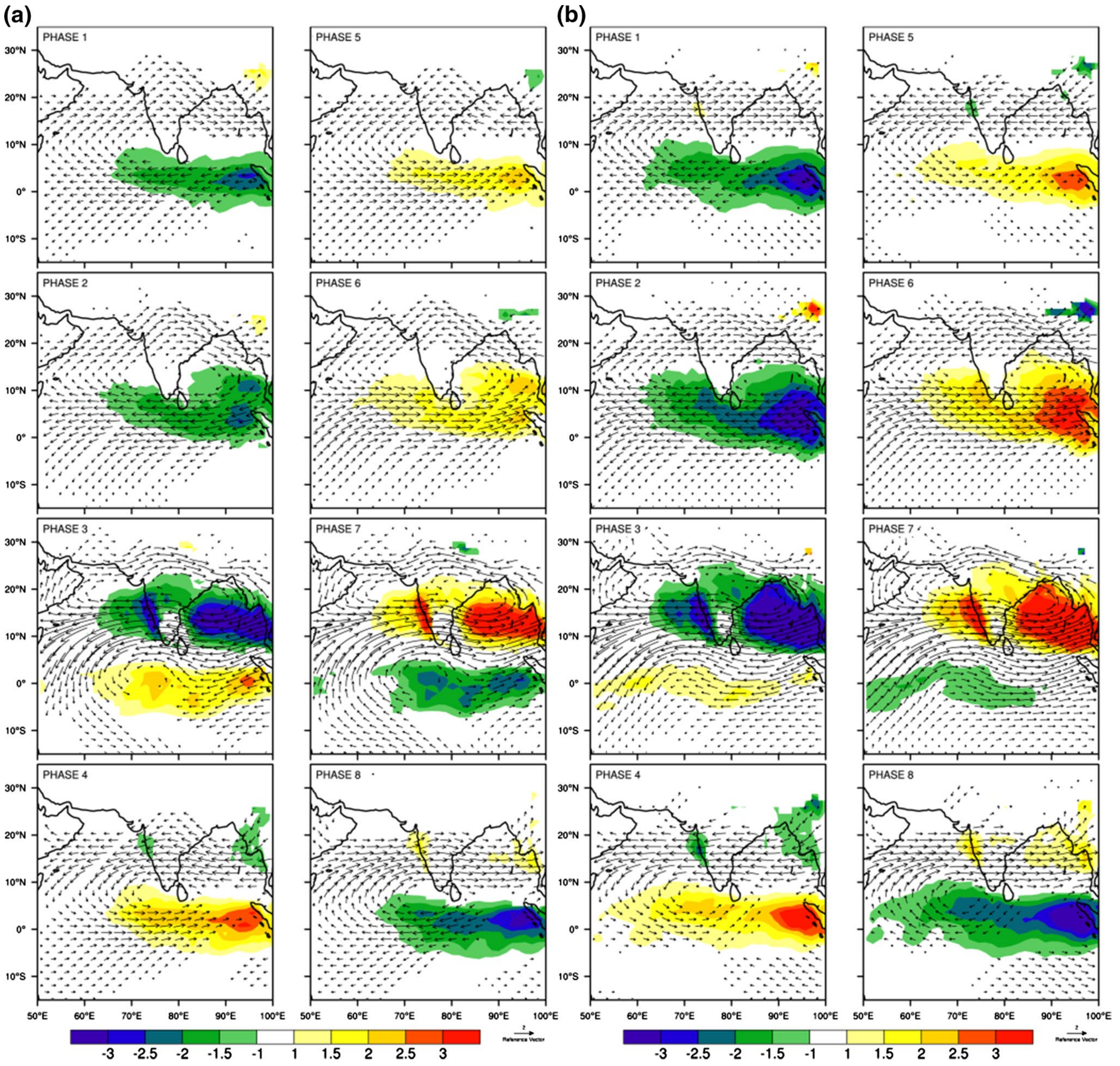

Fig. 10 Composite evolutions of the 30–60-day filtered rainfall (*color scale*, mm day^{-1}) and 850-hPa wind (*vectors*, m s^{-1}) anomalies based on the SADI during a BSISO cycle for phases 1–8 for the period 1 May–31 October from **a** the twentieth century and **b** the twenty-first century simulations. The periods used to calculate are the last twenty years from each century. Only shown are the rainfall and horizontal wind anomalies that are statistically significant at the 5 % significance level. The magnitude of the reference vector is provided at the *bottom right*

of off-equatorial northward propagation is related to the enhanced equatorial signal. However, how the equatorial signal influences the off-equatorial signal deserves further investigation.

The northward-propagating BSISO over the SASM region is characterized by meridional asymmetry of PBL convergence with respect to convection center. This key PBL convergence ahead of convection center could be caused by barotropic vorticity in the free atmosphere (Jiang et al. 2004; Bellon and Sobel 2008). Jiang et al. (2004) proposed an easterly shear mechanism, stating that the seasonal-mean vertical easterly shear causes the generation of barotropic vorticity in the free-atmosphere and the consequent PBL convergence, thus leading to the northward propagation. Bellon and Sobel (2008) suggested that the meridional advection of anomalous baroclinic vorticity by the seasonal-mean meridional baroclinic flow also induces barotropic vorticity north of the convection center. It should

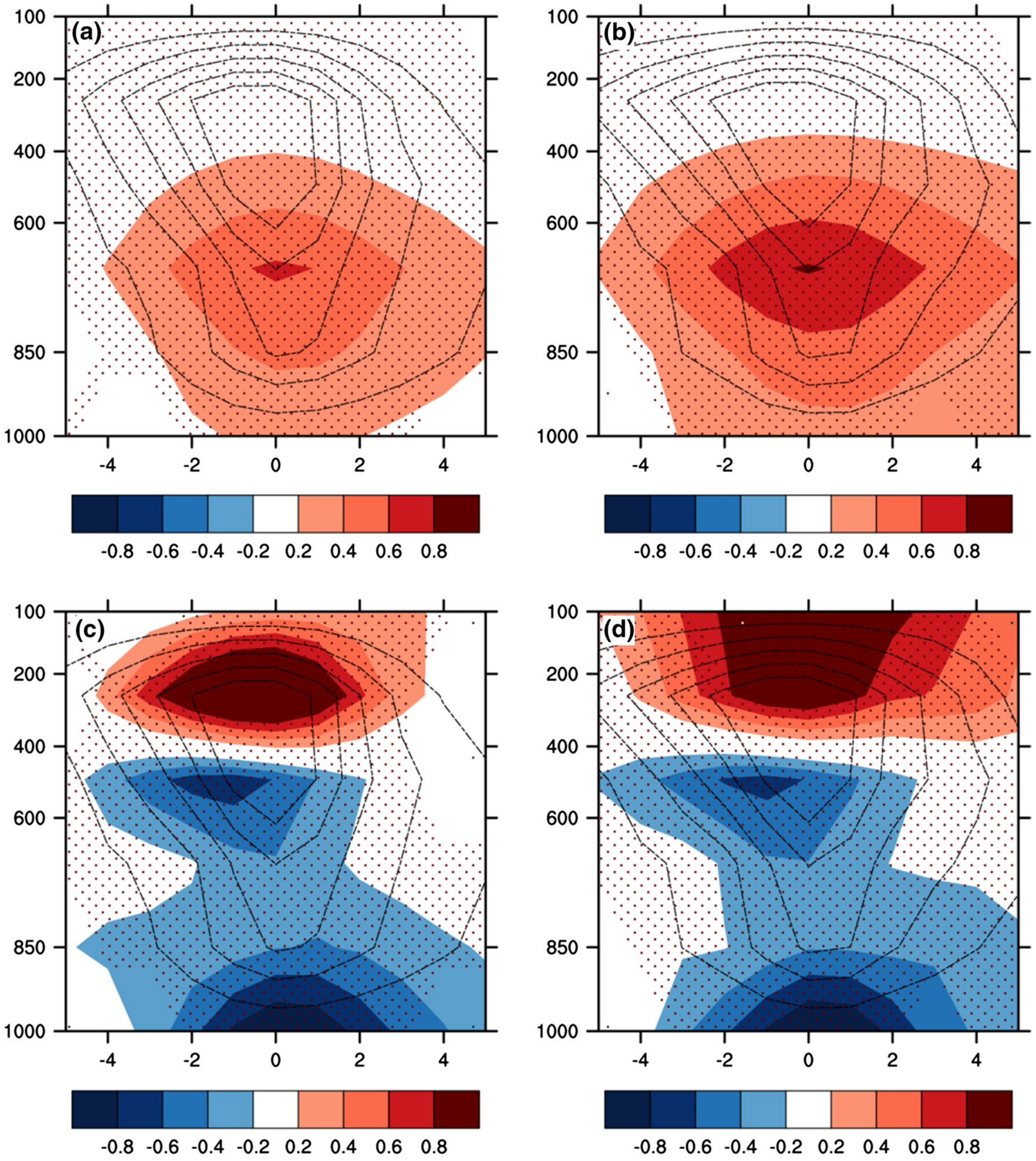

Fig. 11 Meridional-vertical cross sections of anomalous vertical motion (*contour*, 10^{-3} Pa s^{-1}) and specific humidity (*color scale*, g kg^{-1}) regressed against the SADI during the northward propagation of active convection in phases 5–7 for the period 1 May–31 October derived from **a** the twentieth-century and **b** the twenty-first century simulations. **c**, **d** As in (**a**) and (**b**) but for anomalous vertical motion (*contour*, 10^{-3} Pa s^{-1}) and divergence (*color scale*, 10^{-6} s^{-1}). Contours start from -5 and the interval is -5, with only negative values plotted. The *stippling* indicates the regions where either vertical motion or moisture (*divergence*) anomalies are statistically significant at the 5 % significance level. The *horizontal axis* is the meridional distance (expressed as the number of 1.4° grid cells) relative to the convective center, with positive (*negative*) values denoting the north (south) of convective center. The *vertical axis* is pressure (hPa)

be noted that both the vertical easterly shear mechanism and the vorticity advection mechanism are only valid away from the equator (north of 5°N). The northward propagation near the equator results from the low-level moisture advection by the mean or anomalous winds, which is characterized by a positive moisture anomaly located to the north of the convection center. In general, the northward propagation of convection results from low-level moistening and PBL convergence ahead of convection, which are the result of multi-scale interactions between seasonal-mean background and intraseasonal variability. In order to examine whether the above mechanisms are applicable to the simulated northward propagation over the SASM area, we first reconstructed the similar meridional-vertical cross sections of the BSISO-related key variables (vertical motion, specific humidity and divergence) in the northward propagation of active convection (phases 5–7). As the meridional-vertical cross sections at different latitudes were very similar, we composed the meridional-vertical cross sections with respect to the convection center at different latitudes for phases 5–7 (Fig. 11). The ascending motion is observed to coincide with the convection center, with the maximum vertical motion occurring in the middle troposphere (400–600 hPa) (Fig. 11a, c), which results from anomalous convergence in the low-levels and strong anomalous divergence aloft (Fig. 11c). Notice that the convergence in the lower troposphere exhibits a meridional asymmetry, with the convergence covering about 6 latitudes north of the central convection. Although the maximum moisture anomalies occur around the central area of anomalous convection, the area of positive moisture anomaly to the north is larger than that to the south (Fig. 11a). Thus, the presence of low-level convergence and specific humidity meridional asymmetry indicates that the simulated northward propagation over the SASM region may be the combined outcome of easterly vertical shear, vorticity advection and moisture mechanisms.

Because the northward propagation over the SASM is the result of multi-scale interactions, we further examine the changes of season-mean vertical easterly shear (defined as the difference of zonal wind between 100 and 850-hPa), vertical northerly shear (defined as the difference of meridional wind between 100 and 850-hPa), meridional wind in the PBL (defined as the meridional wind averaged between 1000 and 850-hPa), meridional gradient of PBL specific humidity and the associated intraseasonal variations, so as to determine the key physical processes responsible for the modifications of northward propagation. Over the SASM region, the vertical meridional wind shear intensifies significantly in the future climate simulation, with a large magnitude of increase (68 %) in the area-averaged northerly wind shear over SASM area relative to the present-day simulation. However, there is no considerable change in the vertical zonal wind shear, PBL meridional wind or meridional gradient of specific humidity over the SASM area (not shown), with the change rate in each of these factors less than 10 %. Note that the intensified equatorial convection (Figs. 5b, 6b) provides a stronger source for the northward propagation. The enhanced equatorial convection and northerly vertical shear are expected to lead to a stronger barotropic vorticity and PBL convergence ahead of convection through vorticity advection mechanism. However, the PBL convergence north of convection center is strengthened slightly (Fig. 11d), indicating that vorticity advection mechanism is not the main reason for the intensified northward propagation. Notice that the enhanced equatorial convection again strengthens the upward motions at the top of the PBL and the low-level moisture, thus intensifying the amplitude of northward propagation through moisture mechanisms (Fig. 11b).

Note that in response to the warmer SSTs, the moisture-holding capacity of the low-level atmosphere increases during the climatological boreal summer, indicating that it takes more time to accumulate enough moisture anomalies for triggering convections. Therefore, the phase speed is slowed down (Figs. 7b, 8), albeit the amplitudes of northward propagating BSISOs increase.

4.4 Changes in the northward propagation over the EASM region

In this subsection, we discuss the potential impact of global warming under the RCP8.5 scenario on the northward propagation of the 30–60-day BSISO over the EA/WNP region. As shown in Fig. 12, the CNRM-CM5 model properly simulates the northward propagation of anomalous rainfall and zonal wind over the western Pacific longitudes, with the most prominent spectra appearing at meridional numbers 1–2 and periods in the range of 40–80 days (Fig. 12a). Although the 850-hPa zonal wind anomalies also exhibit a southward propagation, the amplitude of the southward propagating component is much weaker than that of the northward propagating counterpart (Fig. 12a). The latitude–time–lag diagram further confirms the northward propagation over the EA/WNP area, with rainfall anomalies leading zonal wind anomalies by 10 days (Fig. 12c). Due to the northward propagation in the EA/WNP section, anomalous convection in the EWP and WNP exhibits a lagged south-north oriented dipole pattern on the 30–60 day timescale (Fig. 9b), with the negative correlation coefficient peaking at the 6-day time lag (Fig. 13). This again implies that the CNRM-CM5 model captures the northward propagation over the EA/WNP region, although the northward-propagating phase speed is overestimated.

In the global warming context, the amplitudes of both rainfall and low-level winds become stronger, indicating the intensification of the coupled convection–circulation system in the northward propagation (Fig. 12b, d). Note that the time lag of the dipole pattern in the EA/WNP area (Fig. 9d) will prolong from 6 to 10 days (Fig. 13), indicating a considerable slow-down of northward propagation under global warming condition.

Based on the above time lag, we defined the model EADIs and constructed composite evolutions of the 30–60-day BSISO during phases 1–8 of the model EADI for the present-day climate (Fig. 14a). When the upstream active convection propagates eastward from the EIO into the Maritime Continent in phase 3, a huge anomalous anticyclone

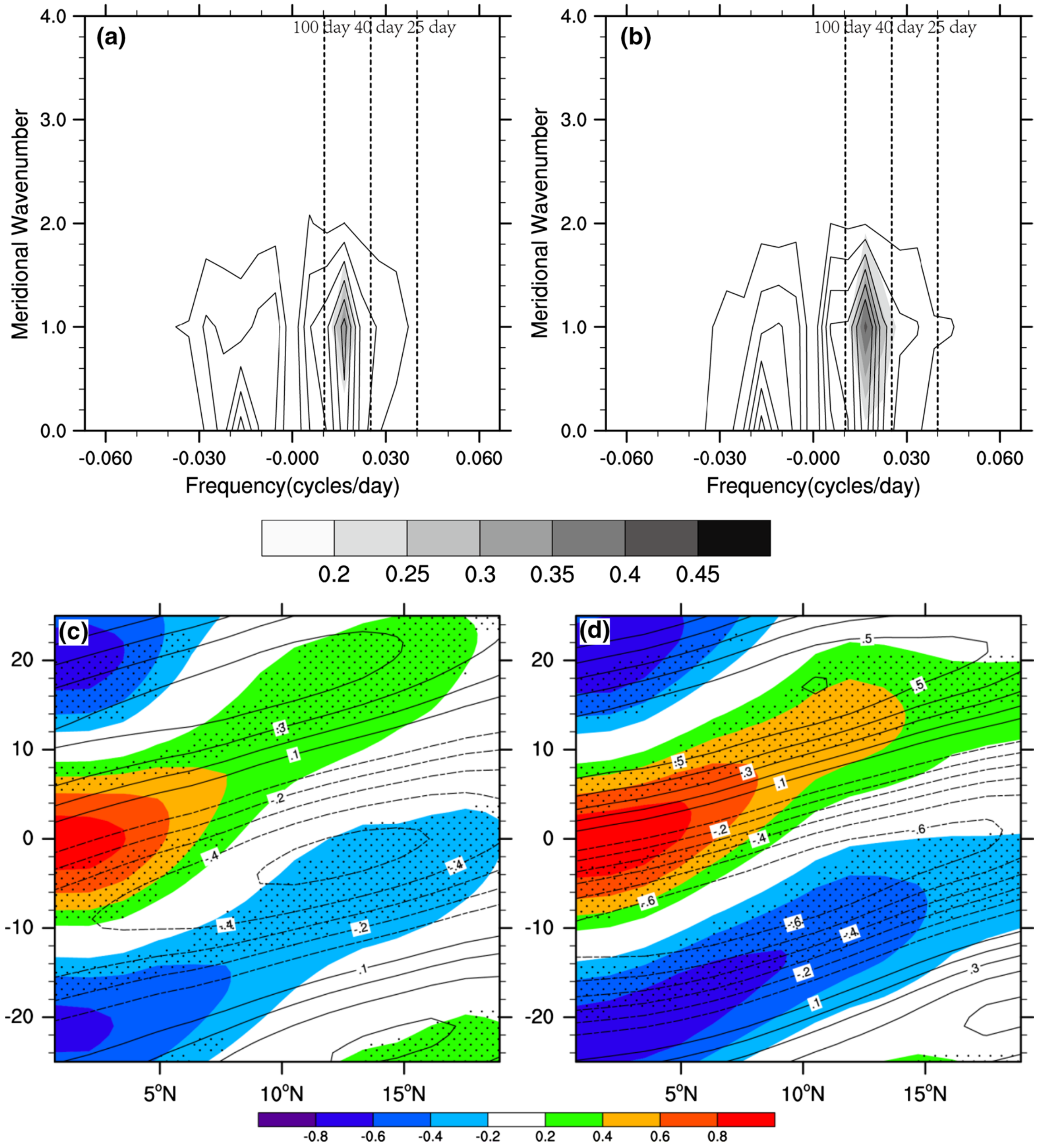

Fig. 12 **a**, **b** As in Fig. 7a, b except for wavenumber-frequency power spectra over the EA/WNP area (10°S–30°N, 100°–140°E). **c**, **d** As in Fig. 7c, d except for northward propagation along the western Pacific longitudes (100°–140°E), with the reference time series as the area-averaged 30–60-day filtered rainfall over the EWP (5°S–5°N, 100°–140°E)

exists to the north of 10°N, dominating a large off-equatorial area from the Indochina peninsula to around 150°E. Note that the anomalous easterlies of the anticyclone are accompanied by suppressed convection. Subsequently, active convection further propagates eastward to the EWP; the suppressed convection and the accompanying anticyclone decay while moving further northward to reach 20°–25°N (phases 4–5). In response to active convection, anomalous westerlies are instead induced over the southern SCS and the Philippines in phase 6, which, together with the anomalous easterlies around 20°N, forms an anomalous cyclone. By phase 7, the anomalous cyclone develops into a dominant system with the strongest active convection, possibly due to the positive feedback between convection and wave dynamics (Gill 1980). Meanwhile, suppressed convection anomalies appear to its south, which actually come from the upstream Indian Ocean. The suppressed convection anomalies will subsequently intensify and migrate

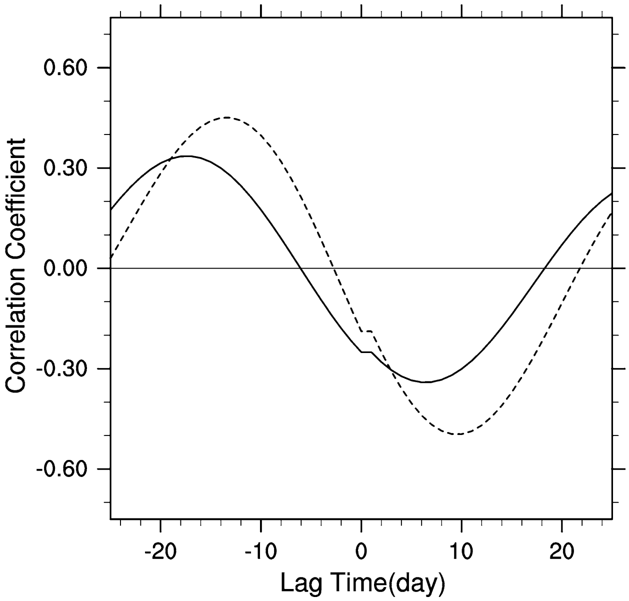

Fig. 13 As in Fig. 8 except for the lead-lag correlation coefficients between area-averaged rainfall anomalies over the EWP (5°S–5°N, 100°–140°E) and over the WNP (10°–20°N, 100°–140°E)

northward in the next cycle. The above composite analysis again indicates that the northward propagation of the 30–60-day BSISO over the EA/WNP region is intimately tied to the equatorial component.

In the twenty-first century under the RCP8.5 scenario (Fig. 14b), the anomalous active (suppressed) convection along with associated low-level zonal wind convergence (divergence) over the EWP becomes much stronger as compared with the historical simulation. In association with the intensified equatorial convection, the northward-propagating cyclone (anticyclone) also intensifies.

To understand what mechanisms are responsible for the modifications of northward propagation over the EA/WNP area in the global warming scenario, we again examine whether the northward propagation mechanisms proposed by Jiang et al. (2004) and Bellon and Sobel (2008) are also applicable for the BSISO over the EA/WNP region. As shown in Fig. 15a, c, for the twentieth century simulation, maximum ascents occur in the middle troposphere (400–600 hPa), coinciding with the convective center, and striking meridional asymmetry exists in the low-level moisture and PBL convergence. It is indicated that the northward-propagating BSISO over the EA/WNP area is also associated with the low-level moisture and PBL convergence ahead of convection center. Note that over the EA/WNP region, the seasonal-mean easterly shear is rather weak and is mostly confined to south of 15°N, while the magnitude of meridional wind shear is twice as large as that in the SASM region (not shown). Therefore, the vorticity advection mechanism predominates over the easterly shear mechanism in the EA/WNP area (Chou and Hsueh 2010).

In the twenty-first century simulation, the enhanced equatorial convection and the associated intensified ascending motion at the top of the PBL, together with the wetter PBL background over the EWP, strengthen the positive moisture anomaly ahead of the convection center through the moisture mechanism (Fig. 15b). Moreover, the EA/WNP northerly vertical shear is strengthened by 13 % in the global warming scenario (not shown). This enhanced meridional baroclinic flow is expected to induce a stronger barotropic mode north of convection through vorticity advection mechanism (Chou and Hsueh 2010), and further lead to an enhanced PBL convergence ahead of central convection. As shown in Fig. 15d, however, the PBL convergence north of central convection will not intensify significantly in the RCP 8.5 run, indicating that the vorticity advection mechanism is not the major reason for the stronger northward propagating signals over the EA/WNP area. Also analyzed are changes of other key background fields (seasonal-mean meridional wind in the PBL, zonal vertical shear and meridional gradient of PBL specific humidity) that influence the northward propagation. There is no significant change in any of these three fields over the EA/WNP region, with the change rate in each of these factors less than 10 %. These indicate that the stronger northward-propagating BSISO in EA/WNP sector may result mostly from the enhanced equatorial convection and wetter PBL through moisture-convection mechanism (Jiang et al. 2004).

In a situation similar to the SASM region, the slower northward propagation over the EA/WNP area also results mainly from the delay of convection occurrence due to increased moisture-holding capacity. Moreover, in the present-day simulation, although the maximum moisture anomalies occur around the central area of anomalous convection, the area of positive moisture anomaly to the north is larger than that to the south (Fig. 15a), indicating significant meridional asymmetry of low-level moisture. Notice that moisture anomaly on both sides of convection center strengthens evidently in the global warming scenario (Fig. 15b), with the magnitude of the increase rate south of convection being larger than that to the north of convection (not shown). This implies that the meridional asymmetry in the low-level specific humidity decreases in the warmed climate. Since moisture-convection mechanism is the dominant mechanism of the BSISO in EA/WNP, this decreased meridional asymmetry of low-level moisture may also contribute to the slower phase speed of northward propagation (Jiang et al. 2004).

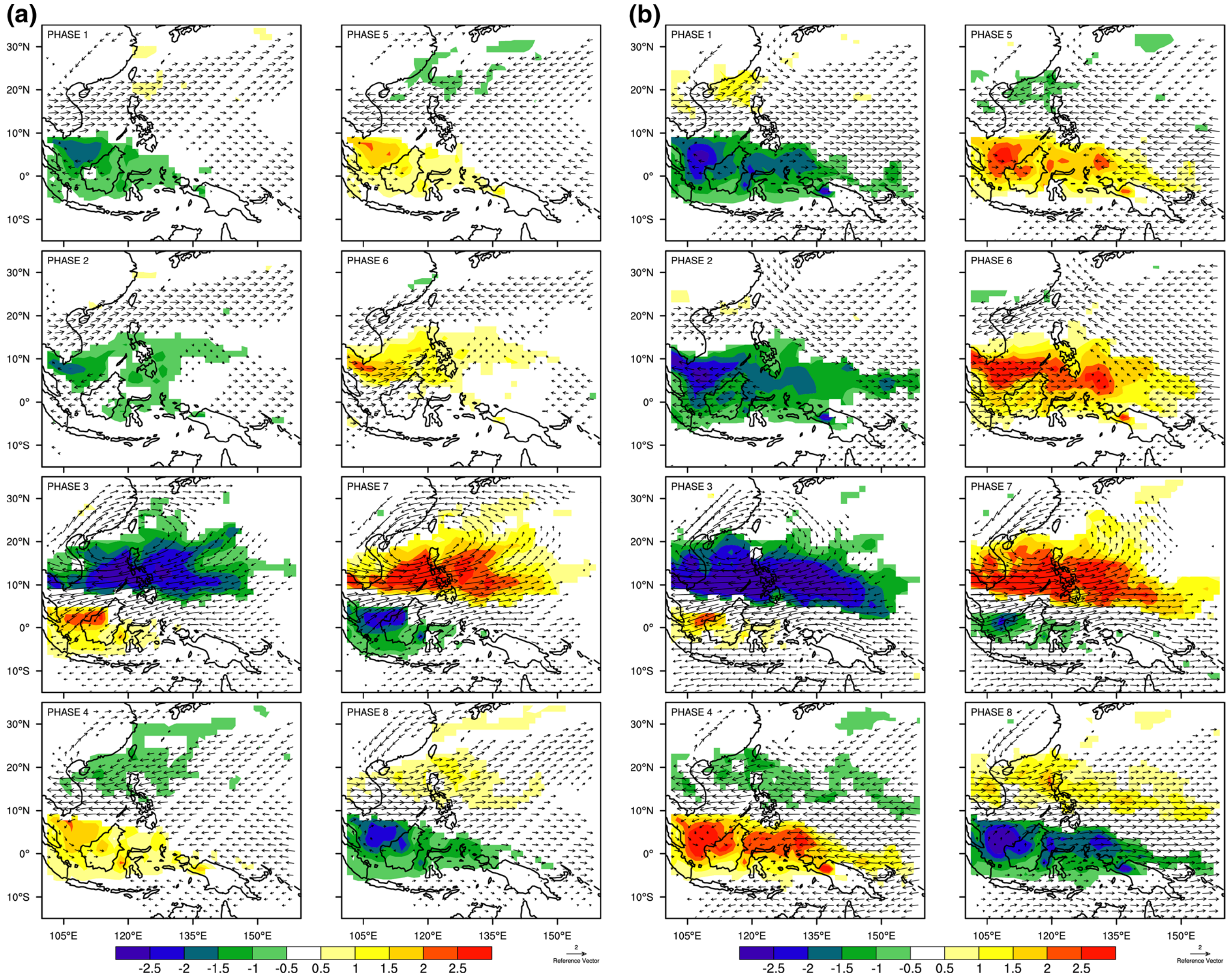

Fig. 14 As in Fig. 10 except for composite evolutions based on the EADI during a BSISO cycle for phases 1–8

5 Summary and discussion

Given that the 30–60-day BSISO is the predominant intraseasonal variability in the ASM region that determines the active and break sequences in rainfall over different sub-ASM areas, especially the SASM and EA/WNP sectors, and it represents the canonical northward and northwestward propagating components over the ASM region in conjunction with the eastward propagating convective anomalies. The objective of this study is to assess possible changes of the 30–60-day BSISO under global warming condition by comparing the twentieth century simulation with the twenty-first century projection under the RCP8.5 scenario, with these simulations derived from the CNRM-CM5 model. The CNRM-CM5 model is capable of simulating both the climatology and intraseasonal variability of the ASM, with a reasonable representation of the 30–60-day BSISO.

From the observations, the 30–60-day BSISO is characterized by a quadrupole convective structure, with two meridional dipole patterns of convection anomalies over the Indian longitudes and the EA/WNP longitudes, respectively. The eastward propagating convective anomalies from the Indian Ocean to the western Pacific connect the upstream dipole with the complementary dipole over the EA/WNP sector. The South Asian Dipole Index (SADI) and the East Asian Dipole Index (EADI) are defined based on the time lag of maximum correlation between the two poles of each dipole convective pattern. In turn, the quadrupole pattern index (QPI) is defined as the difference between the SADI and EADI to represent quadrupole structures of the 30–60-day BSISO and its evolution.

Although the CNRM-CM5 model reproduces the northward propagations over both the SASM and EA/WNP areas, the complementary relationship between the two

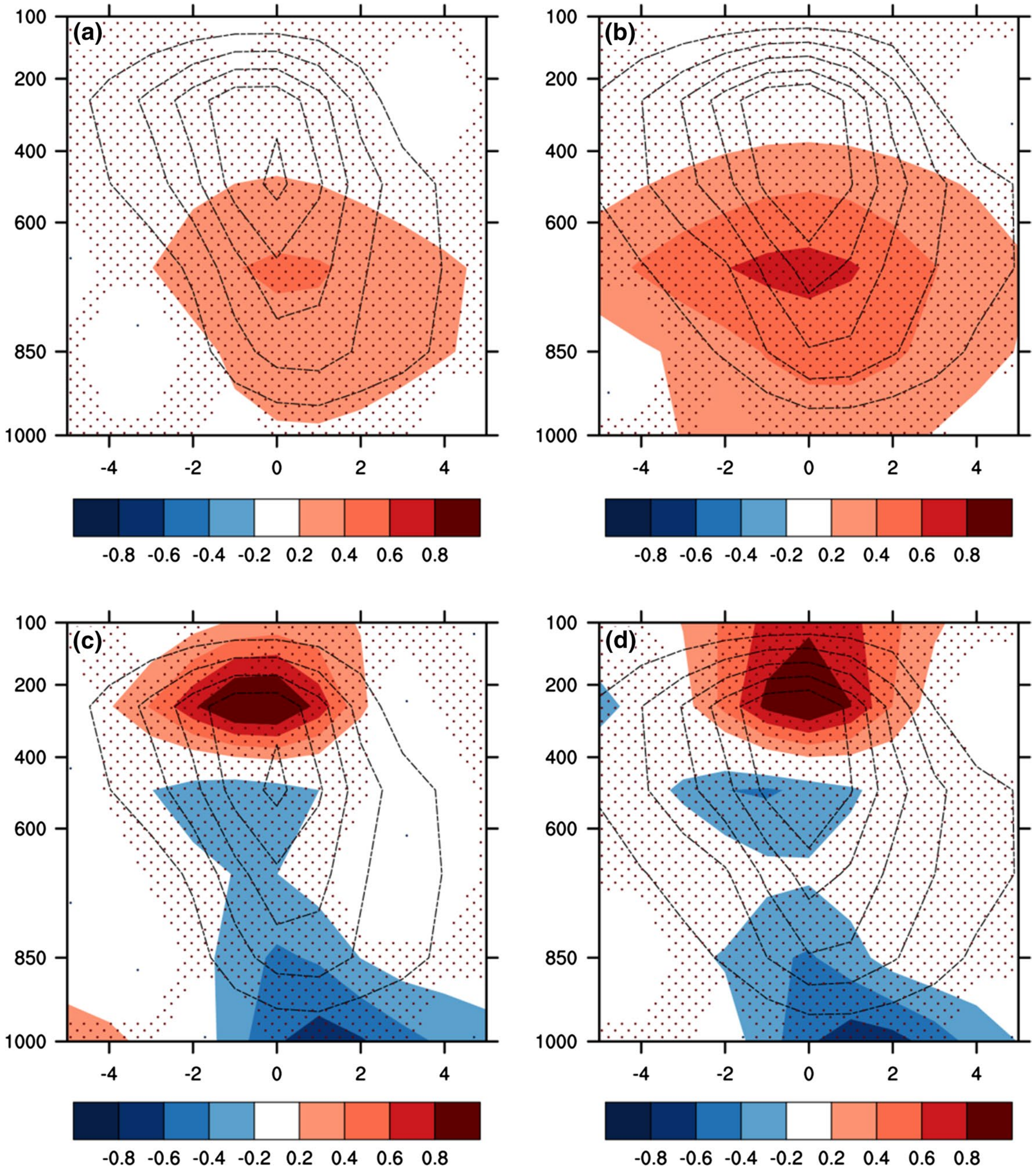

Fig. 15 As in Fig. 11 except for the situations of northward propagation derived from the EADI along the western Pacific longitudes (100°–140°E) during the active phases (phases 5–7)

dipole patterns is not well captured, with the SASM dipole accompanied by convection anomalies with the same sign over the EWP and SCS. Therefore, changes in northward propagation over the SASM and EA/WNP regions are examined with SADI and EADI separately in the present study.

As compared with the BSISO behaviors in the present-day climate, the twenty-first century simulations show that under future global warming conditions, significant changes of the 30–60-day BSISO may take place in terms of amplitude, activity range, and phase speed. The evidently increased variances in 30–60-day rainfall over the EIO, the BOB and the tropical western and central Pacific indicate that the amplitude of the 30–60-day BSISO over these regions may intensify significantly. In response to future warmer SSTs over the tropical Indo-Pacific region, a new equilibrium between the ocean and atmosphere will be established, with the PBL saturation specific humidity increasing by about 16 %, which will provide more moisture and moist static energy for tropical convection.

Consequently, the equatorial frequency-wavenumber power spectra and longitude–time diagram show that the amplitude of eastward propagation intensifies significantly in terms of both rainfall and zonal wind anomalies. Moreover, the 30–60-day BSISO will prevail in a broader area, with the equatorial eastward-propagating convective signals originating over a more westward area in the western Indian Ocean and decaying more eastward to 140°E.

Composite evolutions based on the proposed SADI (EADI) further illustrate that in the global warming scenario, the SASM (EA/WNP) northward-propagating components of the BSISO also strengthen, and they are intimately connected to the enhanced equatorial convective anomalies. The enhanced equatorial convective anomalies accompanied by stronger upward motions at the top of the PBL, together with a wetter seasonal-mean PBL background, cause a stronger positive moisture anomaly ahead of convection through moisture advection mechanism, thus strengthening the northward propagating components. The seasonal-mean northerly wind shear will increase by 68 % (13 %) over the SASM (EASM) region in the warmed climate, which is expected to intensify the northward propagating signals through vorticity advection mechanism. However, the PBL convergence north of convection center is only increased slightly over both two regions, implying the enhanced northerly wind shear do not strengthen the vorticity in the free-atmosphere or the PBL convergence through vorticity advection mechanism. Therefore, it is indicated that the moisture mechanism plays a dominant role over the vorticity advection mechanism in influencing the amplitude of northward propagations.

Moreover, wavenumber-frequency analyses show that the phase speeds of both SASM northward propagation and EA/WNP northward propagation will become slower in the global warming scenario. As the SSTs increase significantly in the tropical Indo-Pacific oceans, the climatological moisture-holding capacity of the low-level atmosphere during the boreal summer will increase, indicating an increase of the moisture threshold for triggering tropical convection. As a consequence, it will take more time to accumulate sufficient moisture anomalies to trigger convection, thus slowing down the evolution of the 30–60-day BSISO over the entire ASM area.

Note that although the CNRM-CM5 model qualitatively reproduces the major behaviors of observed 30–60-day BSISOs, the intensity of the simulated BSISO in the present-day climate is weaker compared with observations (Lee et al. 2013). Similar discrepancies also exist in the seasonal-mean rainfall (Fig. 2a, b). These apparent underestimates of present-day variability may imply that model projections of BSISOs in response to global warming are also underestimated. In the future, we need to verify the above results with other model simulations from CMIP5. While our present study focuses mainly on the roles of atmospheric internal dynamics in causing the modulations of the BSISO in a warmed climate, previous works (e.g., Fu and Wang 2004; Yang et al. 2013; Sabeerali et al. 2014) suggested that air-sea interactions also contribute to enhancing the northward propagation over the SASM area. How the air-sea interactions modify the BSISO evolution over the entire ASM area under the global warming condition demands further investigation. Because the CNRM-CM5 model is unable to well reproduce the 10–20-day oscillation, the present work only investigates the changes of the reasonably represented 30–60-day mode. The modifications of the 10–20-day oscillation by global warming deserve further studies with other models.

Acknowledgments This research was jointly supported by the National Basic Research Program of China (2014CB953902, 2012CB955202, and 2012CB417203), the Priority Research Program of the Chinese Academy of Sciences (XDA11010402), and the Natural Science Foundation of China (91537103, 41375087, and 41175059).

References

Ajayamohan RS, Goswami BN (2007) Dependence of simulation of boreal summer tropical intraseasonal oscillations on the simulation of seasonal mean. J Atmos Sci 64:460–478

Annamalai H, Slingo JM (2001) Active/break cycles: diagnosis of the intraseasonal variability of the Asian summer monsoon. Clim Dyn 18:85–102

Annamalai H, Sperber KR (2005) Regional heat sources and the active and break phases of boreal summer intraseasonal (30–50 day) variability. J Atmos Sci 62:2726–2748

Arakawa A (2004) The cumulus parameterization problem: past, present, and future. J Clim 17:2493–2525

Bellon G, Sobel AH (2008) Instability of the axisymmetric monsoon flow and intraseasonal oscillation. J Geophys Res 113:D07108

Bhat GS (2006) The Indian drought of 2002—a sub-seasonal phenomenon. Quart J Roy Meteorol Soc 132:2583–2602

Bretherton CS, Widmann M, Dymnikov VP, Wallace JM, Blade I (1990) The effective number of spatial degrees of freedom of a time-varying field. J Clim 12:1990–2009

Chen TC, Chen JM (1993) The 10–20-day mode of the 1979 Indian monsoon: its relation with the time variation of monsoon rainfall. Mon Weather Rev 121:2465–2482

Chou C, Hsueh YC (2010) Mechanisms of northward-propagating intraseasonal oscillation—a comparison between the Indian Ocean and the western north Pacific. J Clim 23:6624–6640

Decharme B, Douville H (2006) Introduction of a sub-grid hydrology in the ISBA land surface model. Clim Dyn 26:65–78

Decharme B, Douville H (2007) Global validation of the ISBA subgrid hydrology. Clim Dyn 29:21–37

Ding QH, Wang B (2009) Predicting extreme phases of the Indian summer monsoon. J Clim 22:346–363

Fu XH, Wang B (2004) Differences of boreal summer intraseasonal oscillations simulated in an atmosphere–ocean coupled model and an atmosphere-only model. J Clim 17:1263–1271

Fukutomi Y, Yasunari T (1999) 10–25 day intraseasonal variations of convection and circulation over East Asia and western north Pacific during early summer. J Meteorol Soc Jpn 77:753–769

Gill AE (1980) Some simple solutions for heat-induced tropical circulation. Quart J Roy Meteorol Soc 106:447–462

Goswami BN, Ajayamohan RS, Xavier PK, Sengupta D (2003) Clustering of synoptic activity by Indian summer monsoon intraseasonal oscillations. Geophys Res Lett 30(8):1431. doi:10.1029/2002GL016734

Held IM, Soden BJ (2006) Robust responses of the hydrological cycle on global warming. J Clim 19:5686–5699

Hsu HH, Weng CH (2001) Northwestward propagation of the intraseasonal oscillation during the boreal summer: mechanism and structure. J Clim 14:3834–3850

Hung MP, Lin JL, Wang W, Kim D, Shinoda T, Weaver ST (2013) MJO and convectively coupled equatorial waves simulated by CMIP5 climate models. J Clim 26:6185–6214

IPCC (2013) Summary for policymakers. In: Climate change 2013: the physical science basis. Contribution of working group I to the fifth assessment report of the intergovernmental panel on climate change. Cambridge University Press, Cambridge, United Kingdom and New York

Jiang XA, Li T, Wang B (2004) Structures and mechanisms of the northward propagating boreal summer intraseasonal oscillation. J Clim 17:1022–1039

Jiang XA, Waliser DE, Xavier PK, Petch J, Klingaman NP, Woolnough SJ, Guan B, Bellon G, Crueger T, DeMott C, Hannay C, Lin H, Hu WT, Kim D, Lappen CL, Lu MM, Ma HY, Miyakawa T, Ridout JA, Schubert SD, Scinocca J, Seo KH, Shindo E, Song X, Stan C, Tseng W-L, Wang WQ, Wu TW, Wu XQ, Wyser K, Zhang GJ, Zhu HY (2015) Vertical structure and physical processes of the Madden–Julian oscillation: exploring key model physics in climate simulations. J Geophys Res 120:4718–4748

Jones C, Carvalho LMV (2011) Will global warming modify the activity of the Madden–Julian oscillation? Quart J R Meteorol Soc 137:544–552

Jones C, Carvalho LMV, Higgins RW, Waliser DE, Schemm JKE (2004) Climatology of tropical intraseasonal convective anomalies: 1979–2002. J Clim 17:523–539

Kemball-Cook SR, Wang B (2001) Equatorial waves and air–sea interaction in the boreal summer intraseasonal oscillation. J Clim 14:2923–2942

Ko KC, Hsu HH (2006) Sub-monthly circulation features associated with tropical cyclone tracks over the East Asian monsoon area during July–August season. J Meteorol Soc Jpn 84:871–889

Ko KC, Hsu HH (2009) ISO modulation on the submonthly wave pattern and recurving tropical cyclones in the tropical western north Pacific. J Clim 22:582–599

Kobayashi S, Ota Y, Harada Y, Ebita A, Moriya M, Onoda H, Onogi K, Kamahori H, Kobayashi C, Endo H, Miyaoka K, Takahashi K (2015) The JRA-55 reanalysis: general specifications and basic characteristics. J Meteorol Soc Jpn 93:5–48

Krishnamurti TN, Ardanuy P (1980) The 10 to 20-day westward propagating mode and breaks in the monsoons. Tellus 32:15–26

Lau KM, Yang GJ, Shen SH (1988) Seasonal and intraseasonal climatology of summer monsoon rainfall over East Asia. Mon Weather Rev 116:18–37

Lawrence DM, Webster PJ (2002) The boreal summer intraseasonal oscillation: relationship between northward and eastward movement of convection. J Atmos Sci 59:1593–1606

Lee JY, Wang B, Wheeler MC, Fu XH, Waliser DE, Kang IS (2013) Real-time multivariate indices for the boreal summer intraseasonal oscillation over the Asian summer monsoon region. Clim Dyn 40:493–509

Li J, Mao J, Wu G (2015) A case study of the impact of boreal summer intraseasonal oscillations on Yangtze rainfall. Clim Dyn 44:2683–2702

Liebmann B, Smith CA (1996) Description of a complete (interpolated) outgoing longwave radiation dataset. Bull Am Meteorol Soc 77:1275–1277

Lin J, Weickmann K, Kiladis G, Mapes B, Sperber K, Lin W, Wheeler M, Schubert S, Genio AD, Donner LJ, Emori S, Gueremy JF, Hourdin F, Rasch PJ, Roeckner E, Scinocca JF (2006) Tropical intraseasonal variability in 14 IPCC AR4climate models. Part I: convective signals. J Clim 19:2665–2690

Lin J, Weickman KM, Kiladis GN, Mapes BE, Schubert SD, Suarez MJ, Bacmeister JT, Lee MI (2008) Subseasonal variability associated with Asian summer monsoon simulated by 14 IPCC AR4 coupled GCMs. J Clim 21:4541–4567

Liu P (2013) Changes in a modeled MJO with idealized global warming. Clim Dyn 40:761–773

Madden RA, Julian PR (1971) Detection of a 40–50 day oscillation in the zonal wind in the tropical Pacific. J Atmos Sci 28:702–708

Madden RA, Julian PR (1972) Description of global-scale circulation cells in the Tropics with a 40–50 day period. J Atmos Sci 29:1109–1123

Madec G (2008) NEMO ocean engine. Note du Pole de modélisation, Institut Pierre-Simon Laplace (IPSL), France, No 27 ISSN No 1288-1619

Mao J, Chan JCL (2005) Intraseasonal variability of the South China Sea summer monsoon. J Clim 18:2388–2402

Mao J, Sun Z, Wu G (2010) 20–50-day oscillation of summer Yangtze rainfall in response to intraseasonal variations in the subtropical high over the western North Pacific and South China Sea. Clim Dyn 34:747–761

Mlawer EJ, Taubman SJ, Brown PD, Iacono MJ, Clough SA (1997) Radiative transfer for inhomogeneous atmospheres: RRTM, a validated correlated-k model for the longwave. J Geophys Res 102:16663–16682

Molteni F, Corti S, Ferranti L, Slingo JM (2003) Predictability experiments for the Asian summer monsoon: impact of SST anomalies on interannual and intraseasonal variability. J Clim 16:4001–4021

Neelin JD, Held IM (1987) Modeling tropical convergence based on the moist static energy budget. Mon Weather Rev 115:3–12

Noilhan J, Mahfouf JF (1996) The ISBA land surface parameterization scheme. Global Planet Change 13:145–159

Noilhan J, Planton S (1989) A simple parameterization of land surface processes for meteorological models. Mon Weather Rev 117:536–549

Sabeerali CT, Dandi AR, Dhakate A, Salunke K, Mahapatra S, Rao SA (2013) Simulation of boreal summer intraseasonal oscillations in the latest CMIP5 coupled GCMs. J Geophys Res 118:4401–4420

Sabeerali CT, Rao SA, George G, Rao DN, Mahapatra S, Kulkarni A, Murtugudde R (2014) Modulation of monsoon intraseasonal oscillations in the recent warming period. J Geophys Res 119:5185–5203

Seo KH, SchemmJ-KE Wang W, Kumar A (2007) The boreal summer intraseasonal oscillation simulated in the NCEP Climate Forecast System (CFS): the effect of sea surface temperature. Mon Weather Rev 135:1807–1827

Seo KH, Ok J, Son J-H (2013) Assessing future changes in the East Asian summer monsoon using CMIP5 coupled models. J Clim 26:7662–7675

Sperber KR, Annamalai H (2008) Coupled model simulations of boreal summer intraseasonal (30–50 day) variability, part 1: systematic errors and caution on use of metrics. Clim Dyn 31:345–372

Sperber KR, Annamalai H, Kang LS, Kitoh A, MoiseA Turner A, Wang B, Zhou T (2013) The Asian summer monsoon: an intercomparison of CMIP5 vs. CMIP3 simulations of the late 20th century. Clim Dyn 41:2711–2744

Subramanian A, Jochum M, Miller AJ, Neale R, Seo H, Waliser D, Murtugudde R (2014) The MJO and global warming: a study in CCSM4. Clim Dyn 42:2019–2031

Teng H, Wang B (2003) Interannual variations of the boreal summer intraseasonal oscillation in the Asian-Pacific region. J Clim 16:3572–3584

Trenberth KE (2011) Changes in precipitation with climate change. Clim Res 47:123–138

Turner AG, Annamalai H (2012) Climate change and the South Asian summer monsoon. Nat Clim Change 2:587–595

Valcke S (2006) OASIS3 user guide (prism_2-5). Technical report TR/CMGC/06/73, CERFACS, Toulouse, France

Voldoire A, Sanchez-Gomez E, Salas y Mélia D, Decharme B, Cassou C, Sénési S, Valcke S, Beau I, Alias A, Chevallier M, Déqué M, Deshayes J, Douville H, Fernandez E, Madec G, Maisonnave E, Moine MP, Planton S, Saint-Martin D, Szopa S, Tyteca S, Alkama R, Belamari S, Braun A, Coquart L, Chauvin F (2013) The CNRM-CM5.1 global climate model: description and basic evaluation. Clim Dyn 40:2091–2121. doi:10.1007/s00382-011-1259-y

Waliser DE, Jin K, Kang LS, Stern WF, Schubert SD, Wu MLC, Lau KM, Lee MI, Krishnamurthy V, Kitoh A, Meehl GA, Galin VY, Satyan V, Mandke SK, Wu G, Liu Y, Park CK (2003) AGCM simulations of intraseasonal variability associated with the Asian summer monsoon. Clim Dyn 21:423–446

Wang B, Rui H (1990) Synoptic climatology of transient tropical intraseasonal convection anomalies: 1975–1985. Meteorol Atmos Phys 44:43–61

Wang B, Xie X (1997) A model for the boreal summer intraseasonal oscillation. J Atmos Sci 54:72–86

Webster PJ, Magana VO, Palmer TN, Shukla J, Tomas RA, Yanai M, Yasunari T (1998) Monsoons: processes, predictability, and the prospects for prediction. J Geophys Res 103(C7):14451–14510

Yang J, Bao Q, Wang XC (2013) Intensified eastward and northward propagation of tropical intraseasonal oscillation over the equatorial Indian Ocean in a global warming scenario. Adv Atmos Sci 30:167–174

Yasunari T (1980) A quasi-stationary appearance of 30 to 40 day period in the cloudiness fluctuations during summer monsoon over India. J Meteorol Soc Jpn 58:225–229

Zhang CD (2005) Madden–Julian oscillation. Rev Geophys 43:RG2003. doi:10.1029/2004RG000158